

# FGK Benchmark Stars A new metallicity scale

P. Jofré<sup>1,2</sup>, U. Heiter<sup>3</sup>, C. Soubiran<sup>1</sup>, S. Blanco-Cuaresma<sup>1</sup>, E. Pancino<sup>4,5</sup>, M. Bergemann<sup>6,2</sup>, T. Cantat-Gaudin<sup>7,8</sup>, J.I. González Hernández<sup>9</sup>, V. Hill<sup>10</sup>, C. Lardo<sup>4</sup>, P. de Laverny<sup>10</sup>, K. Lind<sup>6,2</sup>, L. Magrini<sup>11</sup>, T. Masseron<sup>12,2</sup>, D. Montes<sup>13</sup>, A. Mucciarelli<sup>14</sup>, T. Nordlander<sup>3</sup>, A. Recio Blanco<sup>10</sup>, J. Sobeck<sup>15</sup>, R. Sordo<sup>7</sup>, S. G. Sousa<sup>16</sup>, H. Tabernero<sup>13</sup>, A. Vallenari<sup>7</sup>, S. Van Eck<sup>12</sup>, and C. C. Worley<sup>10,2</sup>

(Affiliations can be found after the references)

## ABSTRACT

In the era of large spectroscopic surveys of stars of the Milky Way, atmospheric parameter pipelines require reference stars to evaluate and homogenize their values. We provide a new metallicity scale for the FGK benchmark stars based on their corresponding fundamental effective temperature and surface gravity. This was done by analyzing homogeneously with up to seven different methods a spectral library of benchmark stars. Although our direct aim was to provide a reference metallicity to be used by the Gaia-ESO Survey, the fundamental effective temperatures and surface gravities of benchmark stars of Heiter et al. 2013 and their metallicities obtained in this work can also be used as reference parameters for other ongoing surveys, such as Gaia, HERMES, RAVE, APOGEE and LAMOST.

## 1. Introduction

Unlike in the field of photometry or radial velocities, stellar spectral analyses have lacked up until now a clearly defined set of standard stars spanning a wide range of atmospheric parameters and the Sun has always been the single common reference point for spectroscopic studies of FGK-type stars. The estimate of stellar parameters and abundances by spectroscopy is affected by inaccuracies in the input data, as well as by assumptions made in the model atmospheres and by the analysis method itself. This lack of reference stars other than the Sun makes it very difficult to validate and homogenize a given method over a larger parameter space (e.g. Lee et al. 2008a,b; Allende Prieto et al. 2008b; Jofré et al. 2010; Zwitter et al. 2008; Siebert et al. 2011).

This is especially important with the many Galactic surveys of stellar spectra under development (RAVE, Steinmetz et al. 2006); (LAMOST, Zhao et al. 2006); (APOGEE, Allende Prieto et al. 2008a, Majewski. et al. 2013, in prep.); (HERMES, Freeman 2010); (Gaia, Perryman et al. 2001); (Gaia-ESO, Gilmore et al. 2012). Each of these surveys is developing its own processing pipeline for the determination of atmospheric parameters and abundances, but the different methodologies may lead to a non uniformity of the parameter scales. This is in particular problematic for the metallicities and chemical abundances, which are important for Galactic studies performed via star counts. It is thus necessary to define a common and homogeneous scale in order to link different spectroscopic surveys probing every part of the Galaxy.

Kinematical and chemical analyses have been used to study the Milky Way for over a century (Kapteyn & van Rhijn 1920; Gilmore et al. 1989; Ivezić et al. 2012, e.g.), providing, for example, the evidence of the existence of the Galactic thick disk (Gilmore & Reid 1983), which contains stars having different spatial velocities (e.g. Soubiran 1993; Soubiran et al.

2003), different chemical abundance patterns (Bensby et al. 2004; Ramírez et al. 2007) and ages (e.g. Fuhrmann 1998; Allende Prieto et al. 2006), than the thin disk stars. Similarly, much of our knowledge about the Milky Way halo comes from these kind of studies (Eggen et al. 1962; Helmi 2008, e.g.). A halo dichotomy similar to that of the disk has been subject of discussion (Carollo et al. 2007; Schönrich et al. 2011; Beers et al. 2012), where the outer halo has a net retrograde rotation and is metal-poor, contrary to the inner halo, which is slightly more metal-rich. Moreover, the inner halo is composed mainly of old stars (e.g. Jofré & Weiss 2011), although a number of young stars can be observed, which may be the remnants of early accretion of external galaxies. Evidence for these remnants have been found in stellar surveys like by Belokurov et al. (2006). Schuster et al. (2012) found two chemical patterns in nearby halo stars and claim that they have an age difference, supporting the halo dichotomy scenario.

The analyses of stellar surveys have thus contributed to the general understanding of our Galaxy. The problem arises when one wants to quantify the differences in i.e. chemical evolution and time of formation of all Galactic components, which are needed to understand the Milky Way as a unique body. A major obstacle in solving this problem is that each study, like those mentioned above, choose their own data sets and methods. Homogeneous stellar parameters are therefore crucial in order to put the different Galactic structures in context, where [Fe/H] is of particular importance because it is a key ingredient for the study of the chemical evolution of stellar systems. Relations between the elemental abundance ratios [X/Fe] versus [Fe/H], where X is the abundance of the element X, are generally used as tracers for the chemical evolution of galaxies (e.g. Chiappini et al. 1997; Pagel & Tautvaisiene 1998; Reddy et al. 2003; Tolstoy et al. 2009; Adibekyan et al. 2012, 2013, to name a few). Thus, a good determination of the iron abundance is of fundamental importance.

This has motivated us to search for stars of different FGK types, which we call benchmark stars, whose physical prop-

Send offprint requests to:

Paula Jofré, e-mail: pjoFRE@ast.cam.ac.uk;

Ulrike Heiter, e-mail: ulrike.heiter@physics.uu.se

erties are known, as far as possible, independently from spectroscopy. Knowing their radius, bolometric flux and distance allows us to measure their effective temperature directly from the Stefan-Boltzmann relation and their surface gravity from Newton’s law of gravity. Our sample of benchmark stars consists of 34 stars covering different regions of the Hertzsprung-Russell Diagram, representing thereby the different stellar populations of our Galaxy. It is important to comment that our set of FGK benchmark stars comprises also few M giant stars. We have decided to include them in the complete analysis described in this paper because we have been successful in analyzing them with our methods in a consistent way respect to rest of the FGK stars of our benchmark sample. However, they should not be treated as benchmark for FGK population studies.

In Heiter et al. (2013, in preparation, hereafter Paper I), we describe our selection criteria and the determination of the “direct” effective temperature and surface gravity of the benchmark stars. In Blanco-Cuaresma et al. (2013, in preparation, hereafter Paper II), we present our spectral data of these benchmark stars and how we manage the spectra to build libraries of benchmark stars. This article consists on the determination of the metallicity using a library of benchmark stars compatible with the pipelines developed for the parameter estimation of the UVES targets from the Gaia-ESO public spectroscopic survey. For this purpose, up to seven different methods were employed to perform this spectral analysis, which span from the usage of equivalent widths to synthetic spectra. Since the aim of this work is to provide a new scale for the metallicity, we attempted to homogenize our methods by using common observations, atmosphere models, atomic data and analysis runs.

Although the direct application of the reference metallicity is for the homogenization and the evaluation of the different parameter determination pipelines from the Gaia-ESO Survey, the final set of benchmark star parameters and their spectral libraries will provide the possibility to calibrate spectroscopic astrophysical parameters for large and diverse samples of stars, such as those collected by Gaia, HERMES, LAMOST and RAVE.

The structure of the paper is as follows: In Sect.2, we review the metallicity values available in the literature for the benchmark stars. In Sect.3, we describe the properties of the spectra of benchmark stars, while the methods and analysis structure are explained in Sect. 4. Our results are presented in Sect. 5 with an extensive discussion on the metallicity determination in Sect. 6. The paper concludes in Sect. 7.

## 2. The metallicity of benchmark stars: reviewing the literature

The criteria to select the 34 benchmark stars discussed in this paper can be found in Paper I. Due to their brightness and closeness, almost every benchmark star has been previously studied spectroscopically. Based on the recently updated PASTEL catalogue (Soubiran et al. 2010), metallicity values have been reported in 259 different works until 2012, varying from 57 [Fe/H] measurements in the case of HD140283 to only one measurement for  $\beta$  Ara (Luck 1979), and no measurement at all for  $\psi$  Phe. Figure 1 shows those metallicity values taken from PASTEL for each benchmark star, where in black color we show all metallicities and in red color only those where the  $T_{\text{eff}}$  and  $\log g$  values agree within 100 K and 0.5 dex, respectively, with the fundamental values described in Paper I. Note that the Sun and  $\psi$  Phe are not included in Fig. 1 because they are not in PASTEL (the Sun is not in the PASTEL catalogue because of its lack of static coordinates).

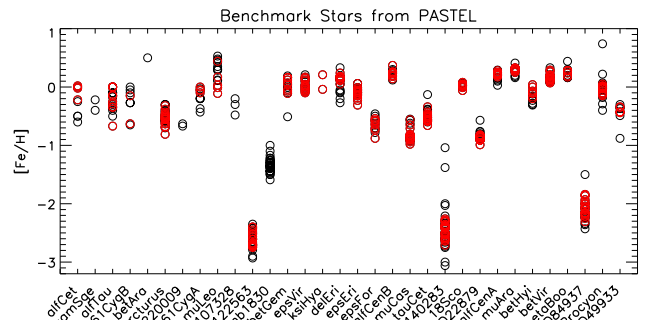


**Fig. 1.** Spectroscopic metallicities reported for the benchmark stars in the literature between 1948 to 2012, as retrieved from the PASTEL database (Soubiran et al. 2010). Black circles: all measurements. Red circles: Only those measurements where  $T_{\text{eff}}$  and  $\log g$  reported by these work agreed within 100 K and 0.5 dex with the values considered by us (see Tab. 1).

Recent studies that have analyzed at least 10 benchmark stars are Allende Prieto et al. (2004), Valenti & Fischer (2005, hereafter VF05), Luck & Heiter (2006a,b), Ramírez et al. (2007, hereafter R07), Bruntt et al. (2010) and Worley et al. (2012, hereafter W12), but none of them have analyzed the complete sample of benchmark stars. The literature value for [Fe/H] that we adopt is the average of the most recent determinations, after 2000, listed in PASTEL. Table 1 gives the mean [Fe/H] with standard deviation and number of values considered after  $3\sigma$  clipping of all references found in PASTEL after 2000. For  $\beta$  Ara the reported value is the only one available, by Luck (1979).

Figure 1 shows how metallicity varies from reference to reference. It is common to have differences up to 0.5 dex for one star. Although the scatter significantly decreases when one considers those works with temperatures and surface gravities agreeing with our values, there are still some stars presenting approx 0.5 dex difference in [Fe/H], like Arcturus and the metal-poor stars HD140283, HD122563 and HD22879. Moreover, by restricting our literature sample by  $T_{\text{eff}}$  and  $\log g$ , we remain without a metallicity value for some of the benchmark stars, such as Gmb 1830,  $\gamma$  Sge and HD107328.

The stars have been plotted in increasing order of temperature,  $\alpha$  Cen being the coldest star and HD49933 the hottest one of our sample. Note that  $\psi$  Phe is colder than  $\alpha$  Cen, but is not plotted in the figure for the reasons explained above. This way of displaying the scatter shows us that cold stars have, firstly, a larger scatter in the metallicity than hot stars. Secondly, there are fewer works providing metallicity for cold stars than for hot stars. This is probably due to the difficulty in analyzing spectra of cold stars.

There are many explanations for the different [Fe/H] values found in the literature, all of them affecting slightly the results, where a combination can lead to the large spread seen in some stars. The methods of determining [Fe/H] in the literature are *highly inhomogeneous*, as they have been carried out by many groups using different assumptions, methodologies, and different sources of data, some of them briefly explained below. An extensive discussion of how these different aspects affect the final parameters of giant stars can be found in Lebzelter et al. (2012), and for solar-type stars in Torres et al. (2012).

- *Methods:* The analysis of the observed spectra can be based on equivalent widths (e.g. Luck & Heiter 2006a,b; Sousa et al. 2008; Taberero et al. 2012, R07) or fitting to synthetic spectra (e.g. VF05, Bruntt et al. 2010). Other techniques than equivalent widths or fitting can be used for deriving

[Fe/H], like the parametrization methods based on projections (Jofré et al. 2010; Worley et al. 2012). Moreover, each method uses a different approach to find the continuum of the spectra.

- *Atomic data*: every work built their line lists using atomic data from different sources, i.e. Bruntt et al. (2010) and VF05 used the VALD database (Kupka et al. 1999) whereas R07 adopted the values given in the NIST<sup>1</sup> database (Wiese et al. 1996). There are also the differential analysis approaches, where the atomic data is adjusted to fit a reference star, typically the Sun (e.g. Santos et al. 2004; Sousa et al. 2008)
- *Observations*: For the same star, different observations are taken and analyzed. For example, Allende Prieto et al. (2004) and R07 studied spectra from the 2coudé instruments (Tull et al. 1995) at the McDonald Observatory and from the FEROS instrument (Kaufer et al. 2000) in La Silla. VF05 used spectra from the spectrometer HIRES (Vogt et al. 1994) at Keck Observatory, UCLES (Diego et al. 1990) at the Siding Spring Observatory and the Hamilton spectrograph (Vogt 1987) at Lick Observatory. Worley et al. (2012) used FEROS spectra. These spectra differ in wavelength range coverage, resolution and flux calibration.
- *Atmosphere models*: Typically, MARCS (Gustafsson et al. 2008, and references therein) and Kurucz (Kurucz 1993) atmosphere models are used equally, which can change the derived abundances by up to 0.1 dex (Allende Prieto et al. 2004; Pancino et al. 2011). In addition, when using three-dimensional (3D) hydrodynamical atmosphere models one can obtain different stellar parameters compared to using one-dimensional (1D) hydrostatic models (e.g. Collet et al. 2007).
- *Solar abundances*: Over the past years, the abundances of the Sun have been updated and therefore metallicities are provided using different zero points. Edvardsson et al. (1993), for example, considered the solar chemical abundances of Anders & Grevesse (1989) while Meléndez et al. (2008) referred to the solar abundances of Asplund et al. (2005).
- *Non-local thermodynamical equilibrium*: NLTE effects can have a severe impact on the abundance determinations, especially for the neutral lines of predominantly singly-ionized elements, like Fe I (Thévenin & Idiart 1999; Asplund 2005; Asplund et al. 2009). The effect is typically larger for metal-poor and giant stars (Thévenin & Idiart 1999; Bergemann et al. 2012; Lind et al. 2012). For this reason, some works make corrections in the abundances (e.g. Thévenin & Idiart 1999; Mishenina & Kovtyukh 2001).

Figure 2 compares the metallicities obtained for the largest common set of benchmark stars analyzed by three different authors, namely by VF05, R07 and W12. This common sample of 12 stars contains 18 Sco,  $\alpha$  Cen A and B,  $\beta$  Hyi,  $\beta$  Vir,  $\delta$  Eri,  $\epsilon$  Eri,  $\epsilon$  For, HD22879,  $\mu$  Ara, Procyon and  $\tau$  Cet, corresponding to stars with high gravities in the benchmark star sample. A systematic offset of +0.05 dex is found in [Fe/H] between VF05 and the other two works, which might be produced partly from the small offset of the temperature and gravities, and partly from the reasons described above. In addition to the observations, atomic data and atmosphere models employed by the two authors, the stellar parameters are determined differently. While R07 uses the Infrared Flux Method with photometric colors to derive temperatures and evolutionary tracks with distances to derive surface

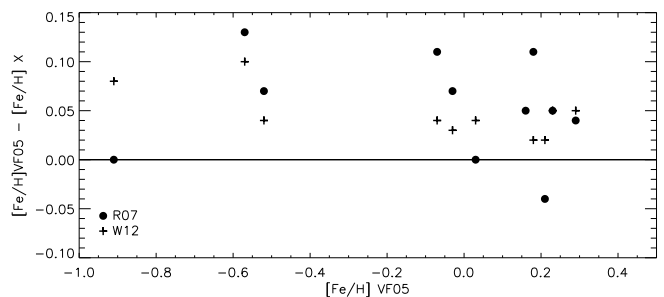


**Fig. 2.** Difference of metallicity for 12 common benchmark stars analyzed in Valenti & Fischer (2005, VF05), Ramírez et al. (2007, R07) and Worley et al. (2012, W12).

gravities, VF05 and W12 derive these parameters directly from the spectra.

Even when making a one-to-one comparison of three parameters for 12 stars of similar spectral type analyzed recently, one cannot control the differences completely and thus one cannot decide which result of parameters is more suitable for reference. Moreover, we can not extrapolate the behavior of the parameters obtained by these two methods to other spectral types, like giants or metal-poor stars.

### 3. Observational Data

The spectra used in this work have very high signal-to-noise (SNR) and high resolution. Since the benchmark stars cover the northern and southern hemisphere (see Paper I for their coordinates), it is not possible to obtain the spectra of the whole sample with one single spectrograph. For that reason we have compiled a spectral library collecting spectra from three different instruments: HARPS, NARVAL and UVES.

The HARPS spectrograph is mounted on the ESO 3.6m telescope (Mayor et al. 2003), and the spectra were reduced by the HARPS Data Reduction Software (version 3.1). The NARVAL spectrograph is located at the 2m Telescope Bernard Lyot (Pic du Midi, Aurière 2003). The data from NARVAL were reduced with the Libre-ESPRIT pipeline (Donati et al. 1997). The UVES spectrograph is hosted by unit telescope 2 of ESO’s VLT (Dekker et al. 2000). Two sources for UVES spectra are considered, the Advanced Data Products collection of the ESO Science Archive Facility<sup>2</sup> (reduced by the standard UVES pipeline version 3.2, Ballester et al. 2000), and the UVES Paranal Observatory Project UVES-POP library (Bagnulo et al. 2003, processed with data reduction tools specifically developed for that library). More details of the observations and properties of the original spectra can be found in Paper II.

To have an homogeneous set of data for the metallicity determination, we have built a spectral library as described in Paper II. The spectra have been corrected to zero redshift. The wavelength range has been reduced to the standard UVES 580 setup, which is from 476 to 684 nm, with a gap from 577 to 584 nm between the red and the blue CCD. We have chosen this range because it coincides with the standard UVES setup employed by the Gaia-ESO Survey and our methods are developed to work in that range. Two libraries of spectra are considered: one with  $R = 70000$ , which is the highest common resolution available in our data, and the other one with original resolution

<sup>1</sup> [http://physics.nist.gov/PhysRefData/ASD/lines\\_form.html](http://physics.nist.gov/PhysRefData/ASD/lines_form.html)

<sup>2</sup> [http://archive.eso.org/eso/eso\\_archive\\_adp.html](http://archive.eso.org/eso/eso_archive_adp.html)

( $R > 70000$ ), which is different for each spectrum and is indicated in Tab. 1. The spectra are not normalized, i.e. each method decided for itself the best way to perform normalization for the determination of the metallicity.

## 4. Method

For consistency, we have used as much common material and assumptions as possible, which are explained below. In this section we also give a brief description of each metallicity determination method considered for this work.

### 4.1. Common material and assumptions

The analysis is based on the principle that the effective temperature and the surface gravity of each star are known. These values (indicated in Tab. 1) are obtained independently from the spectra using fundamental methods, i.e. taking the angular diameter and bolometric flux to determine the effective temperature and the distance to determine surface gravity. In our analysis, we fix  $T_{\text{eff}}$  and  $\log g$  values, as well as rotational velocity (values also indicated in Tab. 1). The latter were taken from the literature, trying to be as homogeneous as possible, for which the source is also indicated in Tab. 1. For those methods where a starting value for the metallicity is needed, we set  $[\text{Fe}/\text{H}] = 0$ .

We used the line list that has been prepared for the analysis of the stellar spectra from the Gaia-ESO survey (Heiter et al. 2013b, in prep, version 3, hereafter GES-v3). The line list includes simple quality flags like “yes” (Y), “no” (N) and “undetermined” (U) which were assigned from an inspection of the line profiles and the accuracy of the  $\log gf$  value for each line based on comparisons of synthetic spectra with a spectrum of the Sun and of Arcturus. If the profile of a given line is well reproduced and its  $\log gf$  flag is well determined, then the line has ‘Y/Y’. On the contrary, if the line is not well reproduced (also due to blends) and the source of  $\log gf$  is not well determined, the line is marked with the flag “N/N”. We considered all lines except those assigned with the flag “N” marked for the atomic data or the line profile. Finally, all methods used the 1D hydrostatic atmosphere models of MARCS (Gustafsson et al. 2008), which consider local thermodynamical equilibrium (LTE), and plane-parallel or spherical symmetry for dwarfs and giants, respectively. These atmosphere models were chosen to be consistent with the pipelines of the Gaia-ESO Survey.

### 4.2. Runs

Three main analyses were made, which are explained below. These runs allow us to study the behavior of our results under different methods, resolutions and instruments.

1. *Run-nodes*: One spectrum per star at  $R = 70000$ , where for stars with more than one spectrum available in our library, the “best” spectrum was selected by visual inspection. The evaluation was mainly based on the behavior of the continuum, but also considered the SNR and the amount of cosmic ray features and telluric absorption lines. The source of the spectra used for this test are indicated in Tab. 1. Hereafter, we call this set of data the “70 k library”. The purpose of this run was to have a complete analysis and overview of the performance of different methods for a well-defined set of spectra.

2. *Run-resolutions*: The same selection of spectra as in *Run-nodes*, but using the original resolution version of the library. This value is indicated in Tab. 1. This run allowed us to make a comparative study of the impact of resolution on the accuracy of the final metallicity. This set of spectra is hereafter called the “Original library”.
3. *Run-instruments*: All spectra contained in the benchmark star library at  $R = 70000$ , i.e. several results for each star. The source of the available spectra for each star (when applicable) is indicated in the last column of Tab. 1. Hereafter we call this data set the “complete 70 k library”. This run gave us a way to study instrumental effects, and to assess the internal consistency of the metallicity values with regard to the spectra being employed.

### 4.3. Nodes method description

In this section we explain the methods considered for this analysis. They vary from fitting synthetic spectra to observe spectra to classical equivalent width (EW) methods. Since this analysis is based on 1D hydrostatic atmosphere models, the microturbulent parameter also needed to be taken into account. We considered the value of  $v_{\text{mic}}$  obtained from the relations of M. Bergemann and V. Hill for the analysis of the targets from the Gaia-ESO Survey (hereafter Berg-Hill relation). Some of the methods determined additionally this parameter simultaneously with  $[\text{Fe}/\text{H}]$  using as initial guess the Berg-Hill relation, while others kept  $v_{\text{mic}}$  fixed by the value obtained from the relation. In the following, we will explain briefly each method individually.

#### 4.3.1. LUMBA

*Code description*: The LUMBA-node (Lund, Uppsala, MPA<sup>3</sup>, Bordeaux, ANU<sup>4</sup>) uses the SME (Spectroscopy Made Easy, Valenti & Piskunov 1996; Valenti & Fischer 2005) code (version 298) to analyse the spectra. This tool performs an automatic parameter optimization using a Levenberg-Marquardt chi-square minimization algorithm. Synthetic spectra are computed by a built-in spectrum synthesis code for a set of global model parameters and spectral line data. A subset of the global parameters is varied to find the parameter set which gives the best agreement between observations and calculations. In addition to the atmosphere models and line list as input, it requires masks containing information on the spectral segments that will be analyzed, the absorption lines that will be fitted, and the continuum regions which are used for continuum normalization. The masks have to be chosen so that it is possible to analyze homogeneously the same spectral regions for all stars. To create the masks, we have plotted the normalized fluxes of all benchmark stars and have looked for those lines and continuum points that are present in all stars. The analysis of the LUMBA node was mainly carried out by P. Jofré, U. Heiter, C. Soubiran, S. Blanco-Cuaresma, M. Bergemann and T. Nordlander.

*Iron abundance determination*: We made 3 iterations with SME: (i) determine only metallicity starting from  $[\text{Fe}/\text{H}] = 0$  and fixing  $v_{\text{mic}}$  and  $v_{\text{mac}}$  by the values obtained from the Berg-Hill relations; (ii) determining  $v_{\text{mic}}$  and  $v_{\text{mac}}$  fixing the  $[\text{Fe}/\text{H}]$  value obtained in the previous iteration (see below); (iii) determination of  $[\text{Fe}/\text{H}]$ , including a correction in radial velocity for each line, using as starting values those obtained in the previous iterations.

<sup>3</sup> Max-Planck-Institut für Astrophysik

<sup>4</sup> Australian National University

**Table 1.** Initial parameters and data information for the benchmark stars. Column description:  $[\text{Fe}/\text{H}]_{\text{LIT}}$  corresponds to the mean value of the metallicity obtained by works between 2000 and 2012 as retrieved from PASTEL (Soubiran et al. 2010), where  $\sigma[\text{Fe}/\text{H}]$  is the standard deviation of the mean and  $N$  represents the number of works considered for the mean calculation (see Sect. 2). Effective temperature and surface gravity are determined from fundamental relation as in Paper I and the rotational velocity  $v \sin i$  is taken from literature, with Ref representing the source of this value. The column Source indicates the instrument used to observe the spectrum in the 70K library (see Sect. 4.2), where N, H, U and U.P denote NARVAL, HARPS, UVES and UVES-POP spectra, respectively. R and SNR represent the resolution and signal-to-noise ratio of the spectra of the original library (see Sect. 4.2), respectively. For stars repeated in the complete 70K library (see Sect. 4.2) the extra source are indicated in the column labeled as “extra spectra”. (\*):Two spectra in HARPS are available for this star with different wavelength calibration. (\*\*): There are many spectra of the Sun taken from different asteroids for HARPS and NARVAL (See Paper II for details of the library)

star ID	$[\text{Fe}/\text{H}]_{\text{LIT}}$	$\sigma[\text{Fe}/\text{H}]$	N	$T_{\text{eff}}$	$\log g$	$v \sin i$	Ref $v \sin i$	Source	R (k)	SNR	extra spectra
18 Sco	0.03	0.03	15	5747	4.43	2.2	Saar	N	80	380	H
61 Cyg A	-0.20	0.11	5	4339	4.43	0.0	Benz	N	80	360	–
61 Cyg B	-0.27	0.00	2	4045	4.53	1.7	Benz	N	80	450	–
$\alpha$ Cen A	0.20	0.07	9	5840	4.31	1.9	Br10	H	115	430	U, H*
$\alpha$ Cen B	0.24	0.04	7	5260	4.54	1.0	Br10	H	115	460	–
$\alpha$ Cet	-0.26	0.23	8	3796	0.91	3.0	Zama	N	80	300	H, U
$\alpha$ Tau	-0.23	0.3	15	3927	1.22	5.0	Hekk	N	80	320	H
Arcturus	-0.54	0.04	11	4247	1.59	3.8	Hekk	N	80	380	H, U, U.P
$\beta$ Ara	0.5	0.00	1	4073	1.01	5.4	Me02	H	115	240	–
$\beta$ Gem	0.12	0.06	5	4858	2.88	2.0	Hekk	H	115	350	–
$\beta$ Hyi	-0.11	0.08	6	5873	3.98	3.3	Re03	U.P	80	650	N, H, U
$\beta$ Vir	0.13	0.05	11	6083	4.08	2.0	Br10	N	80	410	H
$\delta$ Eri	0.13	0.08	13	5045	3.77	0.7	Br10	N	80	350	H, U, U.P
$\epsilon$ Eri	-0.07	0.05	17	5050	4.60	2.4	VF05	U.P	80	1560	H, U
$\epsilon$ For	-0.62	0.12	9	5069	3.45	4.2	Schr	H	115	310	–
$\epsilon$ Vir	0.12	0.03	3	4983	2.77	2.0	Hekk	N	80	380	H
$\eta$ Boo	0.25	0.04	9	6105	3.80	12.7	Br10	N	80	430	H
$\gamma$ Sge	-0.31	0.09	2	3807	1.05	6.0	Hekk	N	80	460	–
Gmb 1830	-1.34	0.08	17	4827	4.60	0.5	VF05	N	80	410	–
HD 107328	-0.30	0.00	1	4590	2.20	1.9	Mass	N	80	380	H
HD 122563	-2.59	0.14	7	4608	1.61	5.0	Me06	N	80	300	H, U, U.P
HD 140283	-2.41	0.10	10	5720	3.67	5.0	Me06	N	80	320	H, U, U.P
HD 220009	-0.67	0.00	1	4266	1.43	1.0	Me99	N	80	380	–
HD 22879	-0.85	0.04	16	5786	4.23	4.4	Schr	N	80	300	–
HD 49933	-0.39	0.07	5	6635	4.21	10.0	Br09	H	115	310	–
HD 84937	-2.08	0.09	13	6275	4.11	5.2	Me06	H	115	480	N, U, U.P
$\xi$ Hya	0.21	0.00	1	5044	2.87	2.4	Br10	H	115	370	–
$\mu$ Ara	0.29	0.04	12	5845	4.27	2.3	Br10	U	105	420	–
$\mu$ Cas A	-0.89	0.04	14	5308	4.41	0.0	Luck	N	80	280	U
$\mu$ Leo	0.39	0.10	4	4433	2.50	5.1	Hekk	N	80	400	–
Procyon	-0.02	0.04	18	6545	3.99	2.8	Br10	U.P	80	760	N, H, U
$\psi$ Phe	–	–	0	3472	0.62	3.0	Zama	U	70	220	–
Sun	0.00	0.00	0	5777	4.43	1.6	VF05	H	115	350	H, N, U**
$\tau$ Cet	-0.53	0.05	17	5331	4.44	1.1	Saar	N	80	360	H

**References.** (Saar) Saar & Osten (1997); (Benz) Benz & Mayor (1984); (Br10) Bruntt et al. (2010); (Zama) Zamanov et al. (2008); (Hekk) Hekker & Meléndez (2007); (Me02) De Medeiros et al. (2002); (Re03) Reiners & Schmitt (2003); (VF05) Valenti & Fischer (2005); (Schr) Schröder et al. (2009); (Mass) Massarotti et al. (2008); (Me06) de Medeiros et al. (2006); (Me99) de Medeiros & Mayor (1999); (Br09) Bruntt (2009)

To validate ionization balance in our method, we have built two sets of masks for Fe I and Fe II separately.

**Broadening parameters:** We estimated the microturbulence and macroturbulence parameters in an additional run with SME. For that, we created a mask including all strong neutral lines with  $-2.5 > \log gf > -4.0$  in the spectral range of our data. This value was chosen because lines in this  $\log gf$  regime are sensitive to  $v_{\text{mic}}$  with SME (Valenti & Piskunov 1996). To determine the broadening parameters we considered the initial values obtained from the Berg-Hill relation and fixed with SME  $T_{\text{eff}}$ ,  $\log g$  and  $[\text{Fe}/\text{H}]$ .

**Discussion:** Although we tried to make the analysis as homogeneous as possible, special treatment was necessary for the

metal-poor stars with  $[\text{Fe}/\text{H}] \leq -0.6$  and for the cold stars with  $T_{\text{eff}} \leq 4100$  K. In the case of the metal-poor stars, a significant number of lines from the line masks were not properly detected resulting in the spectra being incorrectly shifted in radial velocity. Since the library is in the laboratory rest frame, we decided not to make a re-adjustment of the radial velocity for these stars. For the rest of the stars, we corrected by radial velocity to account for shifts of individual lines due to e.g. thermal motions (Molaro & Monai 2012). Cold stars needed a special line mask. In many segments molecular blends were very strong, making it impossible to obtain a good continuum placement and also a good fit between the observed and the synthetic spectra. Moreover, determining iron abundances of blend lines with molecules

that are not included in our line list results in an incorrect estimation of the true iron content of those lines. We looked to each spectrum individually and selected the unblended iron lines.

#### 4.3.2. Nice

*Code description:* The pipeline is built around the stellar parameterization algorithm MATISSE (MATrix Inversion for Spectrum Synthesis) which has been developed at the Observatoire de la Côte d’Azur primarily for use in Gaia RVS<sup>5</sup> stellar parameterization pipeline (Recio-Blanco et al. 2006), but also for large scale projects such as AMBRE (Worley et al. 2012, de Laverny et al 2013) and the Gaia-ESO Survey. MATISSE simultaneously determines the stellar parameters ( $\theta$ :  $T_{\text{eff}}$ ,  $\log g$ , global metallicity [M/H] and global alpha element abundance [ $\alpha$ /Fe]) of an observed spectrum  $O(\lambda)$  by the projection of that spectrum onto a vector function  $B_{\theta}(\lambda)$ . The  $B_{\theta}(\lambda)$  functions are optimal linear combinations of synthetic spectra  $S(\lambda)$  within the synthetic spectra grid. For this work, we adopted the synthetic spectra grid built for the Gaia-ESO survey (de Laverny et al. 2012), by using the GES-v3 line-list and the Berg-Hill microturbulence relation. The analysis done by the Nice group was mainly carried out by C. C. Worley, P. de Laverny, A. Recio-Blanco and V. Hill.

*Iron abundance determination:* The wavelength regions selected for this analysis were based on the Fe line mask used by LUMBA. Continuum regions of minimum 8 Å were set about each accepted Fe line or group of lines.

*Broadening parameters:* Since this method is restricted to fit synthetic spectra from a pre-computed grid,  $v_{\text{mic}}$  was determined from the best fit of spectra computed using the Berg-Hill relation.

*Discussion:* The primary test to be undertaken for this analysis, to hold constant  $T_{\text{eff}}$  &  $\log g$  and allow metallicity to vary, is not fundamentally possible for MATISSE in the current configuration as MATISSE converges on all the parameters simultaneously. The best approximation to this test was to first normalize each observed spectrum to the synthetic spectrum of the grid point closest to the accepted parameters of the star, thereby forcing the observed spectrum into its ideal normalized state. MATISSE does accept a first estimate of the parameters, which were set in this case to the fundamental  $T_{\text{eff}}$  and  $\log g$  and solar [M/H] and [ $\alpha$ /Fe]. However MATISSE then iterates freely through the solution space to converge on the best fit stellar parameters for each star based on this configuration of the synthetic spectra grid.

This additionally a direct comparison of the normalized observed spectrum to the synthetic spectra by  $\chi^2$ -test was carried out. The synthetic spectra were restricted to the appropriate constant  $T_{\text{eff}}$  &  $\log g$  with varying [M/H] and [ $\alpha$ /Fe]. This test did not require the MATISSE algorithm and only provided grid point stellar parameters. However, it was useful as a confirmation of the MATISSE analysis, and also a true test for which  $T_{\text{eff}}$  and  $\log g$  could be held constant allowing metallicity to vary. In addition, this is a useful analysis as a validation of the grid of synthetic spectra available for the Gaia-ESO Survey.

For this configuration of continuum regions about key Fe lines, there was reasonable agreement of the stellar parameters to the accepted values for metal-rich dwarfs for both tests. However the  $\log g$  values in particular were not well determined for low gravity and/or metal-poor stars. For example, the gravity of Arcturus was continually underestimated in both analyses ( $\Delta \log g \sim -0.5$  dex). Three potential sources of this based on the selected spectral regions are: a) the ionization balance is not

well represented for these spectral types due to the small number of Fe II lines; b) strong lines were excluded from the regions, the wings of which are typically good gravity indicators; and c) normalization issues in key sections.

The  $\log g B_{\theta}(\lambda)$  functions do show a lack of strong sensitivity due to a lack of strong features, and a key region of reasonable  $\log g$  sensitivity ( $\sim 5000$  Å to  $5200$  Å) was difficult to normalize accurately due to the spectral feature differences between the observed and synthetic. However, ultimately, MATISSE found the solution for each star that best fit this configuration of the synthetic grid which was confirmed in most cases by the  $\chi^2$ -test. We remind again that the final provided solutions could not be the real ones favoured by MATISSE because of the a-priori fixed  $T_{\text{eff}}$  and  $\log g$ . Some consequences of this fixed analysis for MATISSE are discussed below.

#### 4.3.3. ULB (Université Libre de Bruxelles)

*Code description:* The ULB node uses the code BACCHUS (Brussels Automatic Code for Characterizing High accuracy Spectra), which consists of three different modules designed to derive abundances, EWs, and stellar parameters. The current version relies on an interpolation of the grid of atmosphere models using a thermodynamical structure as explained in Masseron (2006). Synthetic spectra are computed using the radiative transfer code TURBOSPECTRUM (Alvarez & Plez 1998; Plez 2012). This analysis was carried out mainly by T. Masseron and S. Van Eck.

*Iron abundance determination:* In this case, where we do not estimate  $T_{\text{eff}}$  nor  $\log g$ , only the modules for measuring iron abundances and EWs were used. The iron abundance determination module features include local continuum placement (adopted from spectrum synthesis using the full set of lines), cosmic and telluric rejection algorithms, local SNR estimation, and selection of observed flux points contributing to the line absorption. Abundances are derived by comparison of the observation with a set of convolved synthetic spectra with different abundances using four different comparison methods:  $\chi^2$  fitting, core line intensity, synthetic fit, and EWs. A decision tree is made out of those methods to select the best matching abundances.

*Broadening parameters:* Microturbulence velocity was determined in an iteratively way together with the iron abundances. For that, new model atmosphere was taken into account for the possible change in metallicity by adjusting the microturbulence velocity. Additionally, a new convolution parameter for the spectral synthesis encompassing macroturbulence velocity, instrumental resolution and stellar rotation was determined and adopted if necessary.

#### 4.3.4. Bologna

*Code description:* The analysis is based on the measurement of EW. This was done using DAOSPEC (Stetson & Pancino 2008), run through DOOp (Cantat-Gaudin et al, in prep), a program that automatically configures some of the DAOSPEC parameters and makes DAOSPEC run multiple times until the input and output FWHM of the absorption lines converge within a threshold that, for the purpose of this analysis, was set to 3%. The analysis of the Bologna method was mainly carried out by E. Pancino, A. Mucciarelli and C. Lardo.

*Iron abundance determination:* The abundance analysis was carried out with GALA (Mucciarelli et al. 2013), an automatic program for atmospheric parameters and chemical abundances

<sup>5</sup> Radial Velocity Spectrometer

determination from atomic lines, based on the Kurucz suite of programs (Kurucz 2005; Sbordone et al. 2004). Discrepant lines with respect to the fits of the slopes of Fe versus EW, excitation potential, and lambda were rejected with a  $2.5\sigma$  cut, as well as lines with too small or too large EW (depending on the star).

*Broadening parameters:* We looked for the best  $v_{\text{mic}}$  whenever possible, by looking for the solution which minimized the slope of the [Fe/H] vs. EW relation. If for some stars it was not possible to converge to a meaningful value of  $v_{\text{mic}}$  (mostly because not enough lines in the saturation regime were measurable with a sufficiently accurate Gaussian fit), we used the Berg-Holl relations which provided a flat [Fe/H] vs. EW relation.

*Discussion:* Some of the stars, having deep molecular bands or heavy line crowding, had to be re-measured with an exceptionally high continuum order (larger than 30). The stars which needed a fixed input  $v_{\text{mic}}$  were: 61 Cyg A and B,  $\beta$  Ara,  $\epsilon$  Eri, and Gmb 1830.

In many cases, the tabulated  $T_{\text{eff}}$  and  $\log g$  values did not provide a satisfactory ionization equilibrium solution, resulting in an absolute difference between [Fe I/H] and [Fe II/H] larger than 0.10 dex. Cases having moderate differences were:  $\alpha$  Cen B,  $\alpha$  Cen,  $\beta$  Ara, HD107328, HD122563, HD140283, HD220009, HD84937,  $\mu$  Ara, Procyon; while 61 Cyg B and  $\psi$  Phe had differences above 1.50 dex. An extensive discussion on this regard can be found in Sect. 5.4 and Sect. 6.

#### 4.3.5. EPINARBO

*Code description:* The EPINARBO-node (ESO<sup>6</sup>-Padova-Indiana-Arcetri-Bologna) adopts a code, FAMA (Magrini et al. 2013), based on an automatization of MOOG (Sneden 1973, v.2010), which is based on EWs determined in the same way than the Bologna method (see Sect. 4.3.4)<sup>7</sup>. The analysis of this node was mainly carried out by T. Cantat-Gaudin, L. Magrini, A. Vallenari and R. Sordo.

*Iron abundance determination:* For the purpose of determination of metallicity only, we have fixed the effective temperature and surface gravity, and computed  $v_{\text{mic}}$  with the adopted formulas of the Berg-Hill relation. In this way, by keeping these three atmospheric parameters fixed, we have obtained the average of both  $\log n(\text{Fe I})$  and  $\log n(\text{Fe II})$ , discarding those abundances which are discrepant by more than one  $\sigma$  from the average value.

*Broadening parameters:* With the value of metallicity obtained as described above, we have recomputed  $v_{\text{mic}}$ , which is set to minimizing the slope of the relationship between  $\log n(\text{Fe I})$  and the observed EWs. Iteratively, we have repeated the analysis with the new set of atmospheric parameters and, with one  $\sigma$  clipping, we have obtained the final values of  $\log n(\text{Fe I})$  and  $\log n(\text{Fe II})$ .

#### 4.3.6. Porto

*Code description:* The method is based on the excitation and ionization balance of the Fe I and Fe II lines. The EWs are measured automatically using ARES<sup>8</sup> (Sousa et al. 2007) which are

then used to compute individual line abundances with MOOG (Sneden 1973). The analysis of the Porto node was carried out by S.G. Sousa.

*Iron abundance determination:* For this exercise we assumed that the excitation and ionization balance is present. In every iteration we rejected outliers above  $2\sigma$ . We find the final value of [Fe/H] when the input [Fe/H] of the models is equal to the average of the computed line abundances.

*Broadening parameters:* For giants, we computed the micro-turbulence because it depends on [Fe/H], which is a parameter that we initially set to [Fe/H]=0 for all stars. For dwarfs, we utilized the value obtained from the Berg-Hill relation, which is independent on the [Fe/H] of the star.

*Discussion:* The original line list used that was comprised of lines that were found to be stable for an automatic measurement, and the atomic data was recomputed using the Sun as a reference. This standard method is described in more detail in Sousa et al. (2008). For this project the method was adapted such that a new line list had to be compiled based on the Fe I and Fe II lines from the GES-v3 linelist.

It should be also noted that EW measurements are more difficult for cool star spectra due to strong blending effects. The same happened for high rotating stars. Because of these reasons we neglected some of the cool stars present in the sample.

#### 4.3.7. UCM (Universidad Computense de Madrid)

*Code description:* The UCM node relies on EWs employing an automatic code based on some subroutines of STEPAR (Tabernero et al. 2012) to determine the metallicity of a given star in an automated way. Metallicities are computed using the 2002 version of the MOOG code (Sneden 1973). We have modified the interpolation code provided with the MARCS grid to produce an output model readable by MOOG. We also wrote a wrapper program to the MARCS interpolation code to interpolate any required model on the fly.

*Iron abundance determination:* The metallicity is inferred from any previously selected Fe I-Fe II linelist. We iterate until the metallicity from the Fe lines and metallicity of the model are the same. The EW determination of the Fe lines was carried out with the ARES code (Sousa et al. 2007). We follow the approach of Sousa et al. (2008) to adjust the *rejt* parameter of ARES according to the SNR of each spectrum. The other ARES parameters that we employed were *smoother* = 4, *space* = 3, *lineresol* = 0.07, and *miniline* = 2. In addition, we performed a  $3\text{-}\sigma$  rejection of the Fe I and Fe II lines after a first determination of the metallicity, then we re-run our program again without the rejected lines. This analysis was carried out by J. I. González-Hernández, D. Montes, and H. Tabernero.

*Broadening parameters:* For the van der Waals damping prescription, we use the Unsöld approximation multiplied by a factor recommended by the Blackwell group. As in the Porto method, we determined  $v_{\text{mic}}$  only for giants, because the Berg-Hill relation depends on [Fe/H] which was initially set to [Fe/H]=0 for all stars. For dwarfs, we fixed  $v_{\text{mic}}$  by the values obtained from the Berg-Hill relation.

## 5. Results

In this section we discuss the metallicity obtained from the three runs described in Sect. 4.2. This allows us to have a global idea of how each method is performing. We further discuss the impact that our stellar parameters have on the ionization balance, and finally we present the NLTE corrections.

<sup>6</sup> European South Observatories

<sup>7</sup> These measurements were carried out independently from the Bologna ones, with slight differences in the configuration parameters (continuum order, input FWHM, starting radial velocity, and so on), leading to small differences in the returned EW measurements that can be quantified to 1–3%, at most.

<sup>8</sup> The ARES code can be downloaded at <http://www.astro.up.pt/>

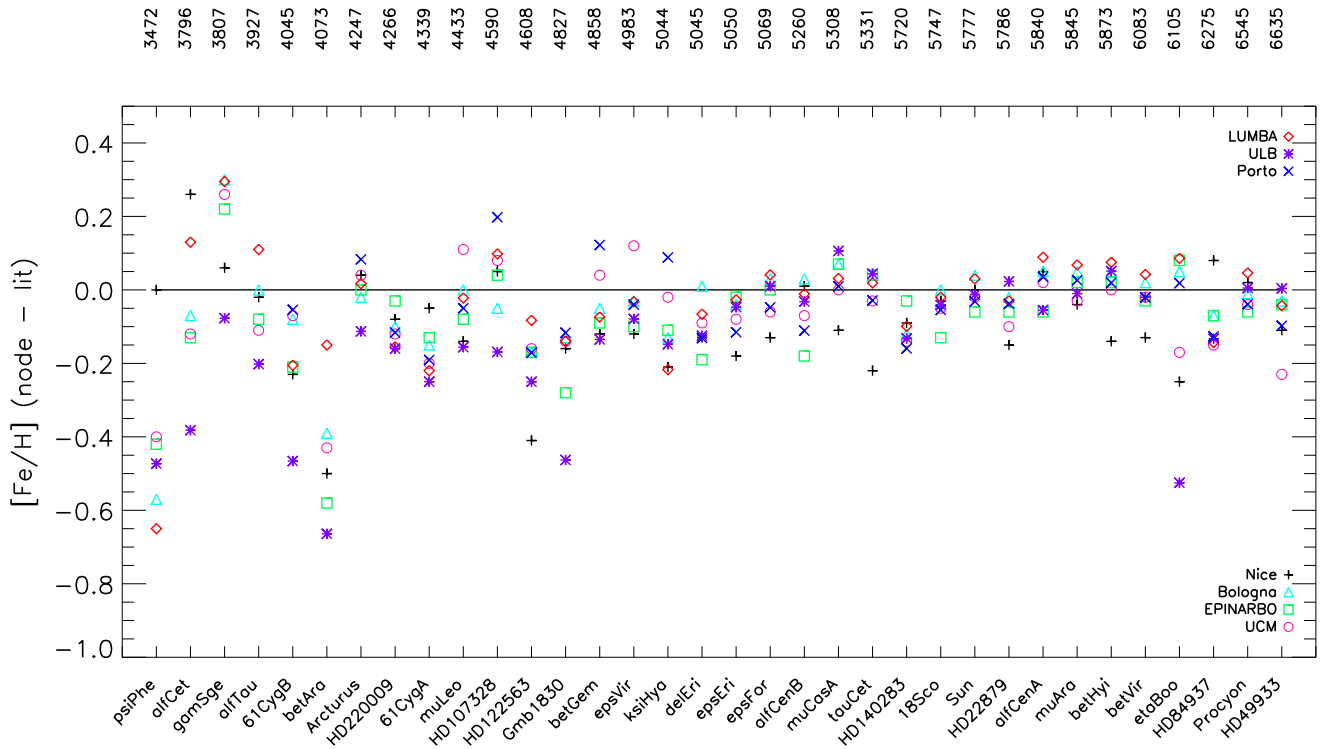


**Fig. 3.** Difference between the metallicity obtained by each node and the mean literature value (see Sect. 2). Stars are plotted as a function of effective temperature. Different symbols correspond to the different methods, which are indicated in the legend.

### 5.1. Comparison of different methods

Table 2 lists the results obtained from *run-nodes*, where every node has determined the metallicity of one spectrum per benchmark star. In Fig. 3 we have plotted the difference between the mean literature value and the result of each node with a different symbol as a function of benchmark star, in increasing order of temperature. The name of the star is indicated at the bottom of the figure, with its corresponding fundamental temperature at the top of it.

For warm stars (i.e.  $T_{\text{eff}} > 5000$  K) the values of metallicity obtained by the different methods have a mean scatter of 0.07 dex. Moreover, these values agree well with the literature, with a mean difference of 0.04 dex. The scatter between different methods increase notably for cold stars, being typically of about 0.1 dex, with a maximum of 0.45 for  $\beta$  Ara. Note that this star has a literature value that was determined from photometric plates (Luck 1979) and is thus uncertain. A similar behavior can be seen in Fig. 1 with the values reported in the literature, where  $[\text{Fe}/\text{H}]$  of cold stars present more scatter than hot stars. The fact that obtaining a good agreement in  $[\text{Fe}/\text{H}]$  for cold stars is more difficult than for warm stars is mainly due to line crowding and the presence of molecules in the spectra of very cold stars. This means that the iron lines in most of the cases are not well recognized nor well modeled. Moreover, absorption lines in cold stars can be very strong, making the continuum normalization procedure extremely challenging. Also, 3D effects can become important in giants (e.g. Collet et al. 2007; Chiavassa et al. 2010) and our models consider only 1D.

Note that for some stars, like  $\beta$  Ara, 61 Cyg A and B, Gmb 1830 and HD122563, we obtain a fair agreement in metallicity. The mean value, however, differs significantly to the mean literature one. In Sect.2 we have discussed how the  $[\text{Fe}/\text{H}]$  from the different works can differ significantly due to inhomogeneities coming from the different methods and input data con-

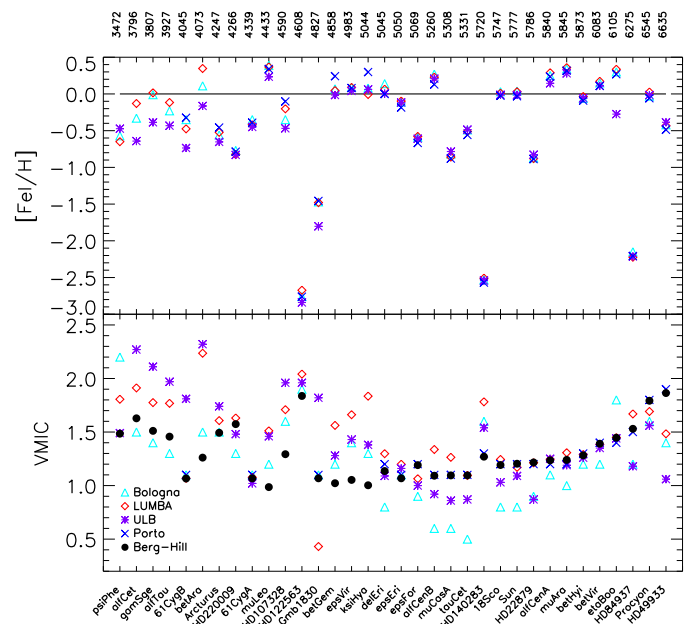


**Fig. 4.** Metallicity (upper panel) and microturbulence velocity (lower panel) obtained by different methods for each benchmark star, as a function of temperature. Black dots correspond to the values of  $v_{\text{mic}}$  obtained from the WG11 relation of Bergemann and Hill.

sidered. A more detailed discussion of each star, especially those with new values, can be found in Sect. 6.2.

When using 1D static models to determine parameters we need to employ additional broadening parameters (micro- and macroturbulence velocity), which represent the non-thermal motions in the photosphere. Since these motions are not described in 1D static atmosphere models, broadening parameters become important to compensate for the effects of these motions. Fig-

**Table 2.** Metallicity of benchmark stars obtained individually by each method.

star	LUM	BOL	EPI	Nice	UCM	ULB	Por
18 Sco	0.01	0.03	-0.10	0.00	-0.02	-0.01	-0.02
61 Cyg A	-0.42	-0.35	-0.33	-0.25	-0.40	-0.45	-0.39
61 Cyg B	-0.47	-0.35	-0.48	-0.50	-0.34	-0.74	-0.32
$\alpha$ Cen A	0.29	0.25	0.14	0.25	0.22	0.14	0.23
$\alpha$ Cen B	0.23	0.27	0.06	0.25	0.17	0.21	0.13
$\alpha$ Cen	-0.13	-0.33	-0.39	0.00	-0.38	-0.64	–
$\alpha$ Tau	-0.12	-0.23	-0.31	-0.25	-0.34	-0.43	–
Arcturus	-0.52	-0.56	-0.54	-0.50	-0.50	-0.65	-0.46
$\beta$ Ara	0.35	0.11	-0.08	0.00	0.07	-0.16	–
$\beta$ Gem	0.05	0.07	0.03	0.00	0.16	-0.01	0.24
$\beta$ Hya	-0.04	-0.06	-0.09	-0.25	-0.11	-0.06	-0.09
$\beta$ Vir	0.17	0.15	0.10	0.00	0.11	0.11	0.11
$\delta$ Eri	0.06	0.14	-0.06	0.00	0.04	0.00	0.00
$\epsilon$ Eri	-0.10	-0.11	-0.09	-0.25	-0.15	-0.12	-0.19
$\epsilon$ For	-0.58	-0.59	-0.62	-0.75	-0.68	-0.61	-0.67
$\epsilon$ Vir	0.09	0.09	0.02	0.00	0.24	0.04	0.08
$\eta$ Boo	0.34	0.30	0.33	0.00	0.08	-0.28	0.27
$\gamma$ Sge	-0.01	-0.01	-0.09	-0.25	-0.05	-0.39	–
Gmb 1830	-1.48	-1.47	-1.62	-1.50	-1.48	-1.80	-1.46
HD107328	-0.20	-0.35	-0.26	-0.25	-0.22	-0.47	-0.10
HD122563	-2.67	-2.76	-2.76	-3.00	-2.75	-2.84	-2.76
HD140283	-2.51	-2.53	-2.44	-2.50	-2.55	-2.54	-2.57
HD220009	-0.82	-0.77	-0.70	-0.75	-0.79	-0.83	-0.79
HD22879	-0.88	-0.87	-0.91	-1.00	-0.95	-0.83	-0.89
HD49933	-0.43	-0.42	-0.43	-0.50	-0.62	-0.39	-0.49
HD84937	-2.22	-2.15	-2.15	-2.00	-2.23	-2.21	-2.21
$\xi$ Hya	-0.01	0.08	0.10	0.00	0.19	0.06	0.30
$\mu$ Ara	0.36	0.34	0.31	0.25	0.26	0.28	0.32
$\mu$ CasA	-0.86	-0.82	-0.82	-1.00	-0.89	-0.78	-0.88
$\mu$ Leo	0.37	0.39	0.31	0.25	0.50	0.23	0.34
Procyon	0.03	-0.03	-0.08	0.00	-0.06	-0.01	-0.06
$\psi$ Phe	-0.65	-0.57	-0.42	0.00	-0.40	-0.47	–
Sun	0.03	0.04	-0.06	0.00	-0.02	-0.01	-0.03
$\tau$ Cet	-0.51	-0.49	-0.49	-0.75	-0.56	-0.49	-0.56

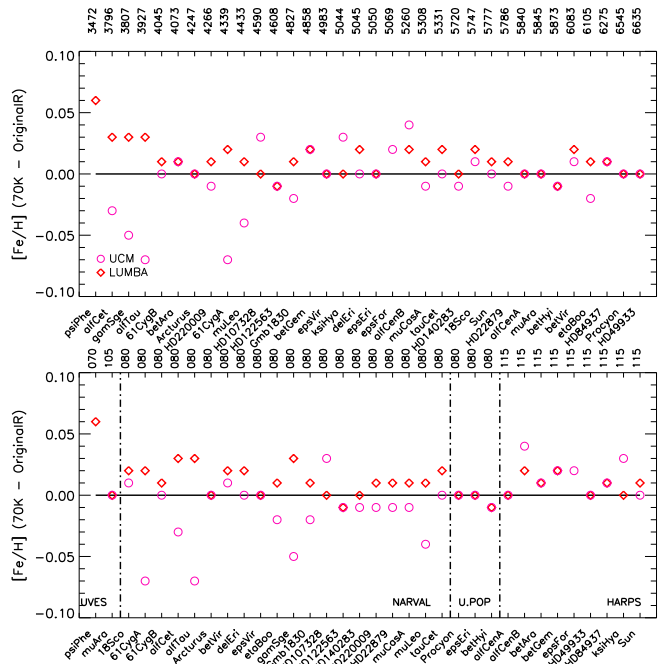
ure 4 shows the correlation between  $[\text{Fe}/\text{H}]$  and  $v_{\text{mic}}$  for the Bologna, LUMBA, ULB and Porto methods. Nissen (1981) made an analysis of  $v_{\text{mic}}$  as a function of  $[\text{Fe}/\text{H}]$ ,  $T_{\text{eff}}$  and  $\log g$  for solar-type dwarfs obtaining a relation where  $v_{\text{mic}}$  increases as a function of  $T_{\text{eff}}$ , which agrees with our results of  $v_{\text{mic}}$  shown in Fig. 4 for warm stars ( $T_{\text{eff}} \geq 5000$  K). This effect has also been noticed in Luck & Heiter (2005) and Bruntt et al. (2012). Metal-poor stars are outliers of the smooth relation, with HD140283 being the most evident one. Such metal-poor stars were not included in the samples of Nissen (1981) and Bruntt et al. (2012). The microturbulence velocity decreases as function of  $T_{\text{eff}}$  for stars colder than  $T_{\text{eff}} \sim 5000$  K, although with a larger scatter than for warm stars. This general behavior agrees with the relations obtained by the Berg-Hill relation (see Sect. 4.3), which is plotted with black dots in Fig. 4.

Note that although each method shows the same behavior of  $v_{\text{mic}}$  as a function of temperature, the absolute value of  $v_{\text{mic}}$  differs. The differences found between methods in  $v_{\text{mic}}$  help to achieve a better general agreement of  $[\text{Fe}/\text{H}]$ . Figure 4 shows us the different dependency of this broadening parameter for our methods.

## 5.2. Comparison of different resolutions

In Fig. 5 we have plotted the comparison of the results from LUMBA and UCM obtained for  $[\text{Fe}/\text{H}]$  when considering the 70 k and original library.

As in previous figures, we illustrate the difference in metallicity as a function of benchmark star, in order of increasing temperature in the upper panel. In the lower panel of Fig. 5 we


**Fig. 5.** Difference of metallicity obtained from 70K and Original library for UCM and LUMBA methods. Upper panel: difference as a function of benchmark star temperature. Lower panel: difference for stars of same instrument.

have plotted together the stars observed with the same instrument. Different instruments are separated by the dashed line. The value of the spectral resolution before convolution is indicated at the top of the figure.

It is interesting to comment on the result of  $\psi$  Phe, which has the lowest original resolution and is the coldest star, because we obtain the largest difference. In the case of the LUMBA method, the synthetic spectra produced by SME need to have a given resolution, which is set to be constant along the entire spectral range. This is, in the original spectra, not completely true. In this particular case, the lower arm of the UVES spectrum has a resolution of 70,000 while the upper arm has a resolution of 65,000 (see Paper II). In any case, the difference is of about 0.06 dex, which is negligible compared to the uncertainty obtained for this star of about 0.5 dex (see Tab. 3 and Sect. 6).

The same can happen for the results from the original NARVAL spectra, which we assume to be  $R = 80,000$ . As discussed in Paper II, the resolution of NARVAL spectra depends on the observing night and might not be exactly 80,000. Moreover, the resolution changes along the NARVAL wavelength range. We have shown in Paper II that when convolving the spectra, the initial resolution does not impact significantly the final profile, therefore it is acceptable to assume  $R = 80,000$  for all the original spectra for creating the 70k library. However, when analyzing directly the original spectra with SME, the exact resolution is not given which might affect the results, explaining the scatter around the zero line observed in Fig. 6 for NARVAL spectra. For a discussion of the impact of parameters when the exact resolution of spectra is not given can also be found in Wu et al. (2011). UVES-POP spectra, on the other hand, have a well defined original resolution and our results agree very well. Finally, HARPS spectra have also a quite well established original resolution. It is also the highest resolution of our sample.

It is worth to comment the results obtained by UCM for cold stars, where the difference between original and convolved spectra are larger than for warm stars. This effect can be attributed

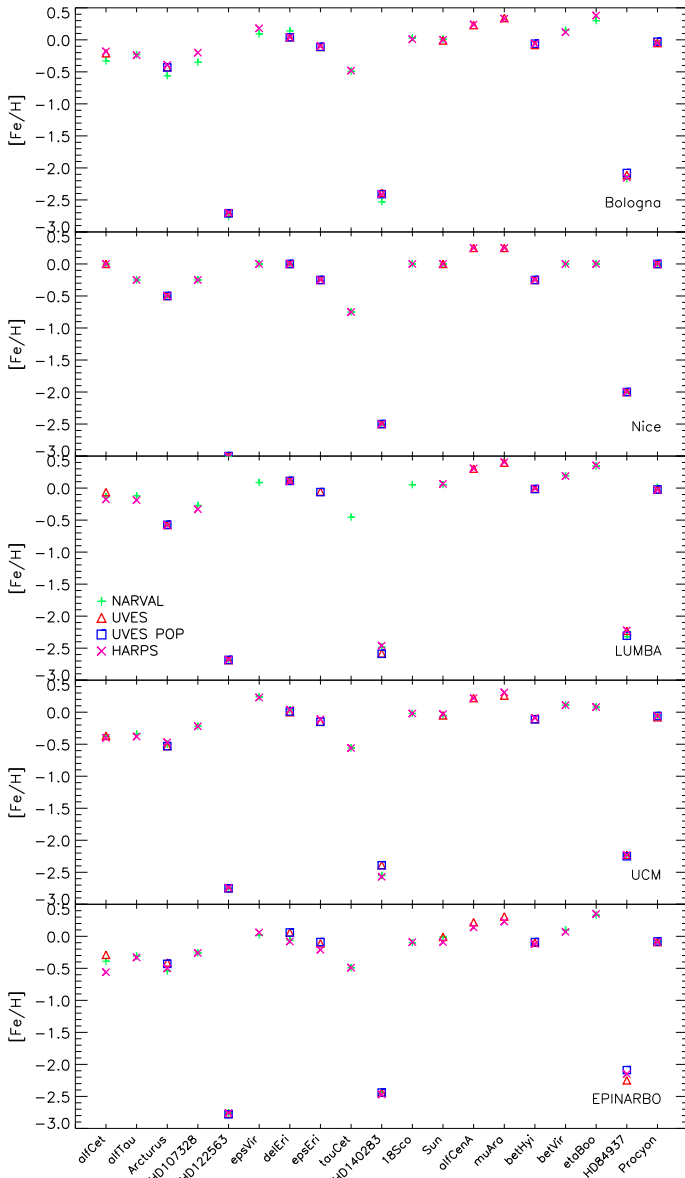


**Fig. 6.** Metallicity of benchmark star as a function of effective temperature. Symbols represent different instruments (see legend). Each panel shows the result of one method, indicated in each panel.

to the contribution of other lines than Fe that can be better resolved at higher resolution, producing a slightly different measurement of the EW. In general, differences of less than 0.03 dex are present for both methods when using different resolutions (and SNR), which is within the errors obtained in the abundances (see Sect. 6).

### 5.3. Comparison of different instruments

For many of the benchmark stars, we have more than one observation. We expect our results to be consistent under different instruments. For that reason, we have determined  $[\text{Fe}/\text{H}]$  for each spectrum separately and have compared them. The results obtained for the methods of Nice, Bologna, EPINARBO, UCM, and LUMBA are displayed in Fig. 6. The plots represent the value of the metallicity as a function of benchmark star, in increasing temperature.

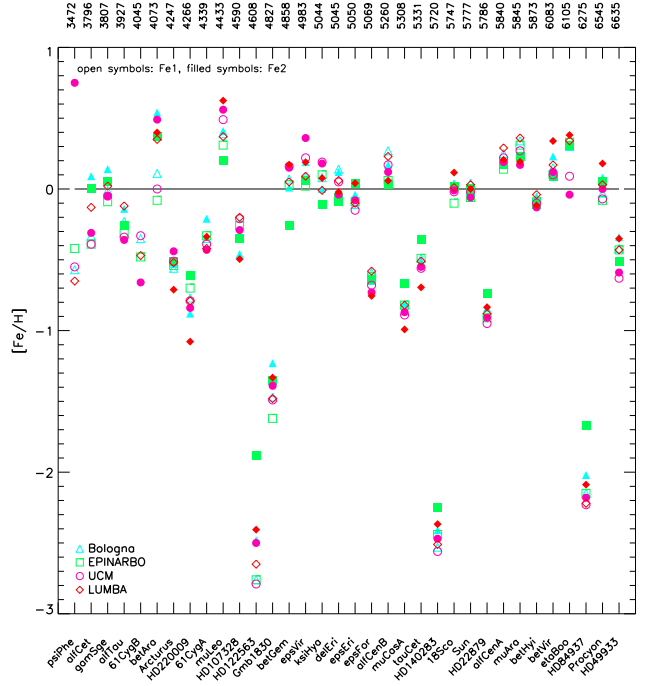


**Fig. 7.** Neutral and ionized iron abundances obtained for benchmark stars as a function of effective temperature by different methods (see legend). Open symbols represent Fe I abundances while filled symbols represent Fe II abundances.

There is a general good agreement when different spectra are analyzed for the same star. Procyon, which has observations in every instrument from our library, has an excellent agreement for each method considered here. On general, our results and data are consistent because we do not find signatures of one particular instrument giving systematic differences. In the same way, we do not find the result of one particular star being biased towards one observation.

This comparison also shows the robustness of our software employed to create the library of benchmark star spectra (Paper II), since different methods are able to analyze these data and obtain consistent results.

### 5.4. Self consistency and ionization balance

Usually, when determining parameters, a compromise is found between  $T_{\text{eff}}$ ,  $\log g$ ,  $v_{\text{mic}}$  (and  $v_{\text{mac}}$  in case of synthetic spectra) and  $[\text{Fe}/\text{H}]$ , so that the iron abundance obtained from neutral lines agrees with that obtained from ionized lines, the so-called ionization balance. Similar relations are used to find the best  $T_{\text{eff}}$  (a flat trend of Fe I with excitation potential) and  $v_{\text{mic}}$  (a flat trend of Fe I with EW).

In this particular work, where we do not change  $T_{\text{eff}}$  and  $\log g$  in order to retrieve self-consistent iron abundances, the simultaneous determination of the other parameters becomes crucial. For methods based on EWs,  $v_{\text{mic}}$  helps to obtain abundances in a line-to-line approach that does not depend on the reduced EW or wavelength range. For methods based on synthetic spectra,  $v_{\text{mic}}$  is treated as a broadening parameter that helps to improve the fit of the synthesis to observed line profiles.

Since  $T_{\text{eff}}$  and  $\log g$  are taken from fundamental relations and are independent of spectral modeling, ionization balance and the mentioned relations tell us how well our models are able to reproduce our observations. Figure 7 displays the iron content ob-



tion balance in each method. The results of this "free" analysis are illustrated in Fig. 9, where the difference between the "fixed" (determination of  $[\text{Fe}/\text{H}]$  via fixing  $T_{\text{eff}}$  and  $\log g$ ) and the "free" analysis are shown for each benchmark star. Metallicity, temperature and surface gravity are plotted in the upper, middle and lower panel of Fig. 9, respectively.

As expected, the metallicity obtained when forcing ionization equilibrium for 1D LTE models is different from that obtained with the fundamental  $T_{\text{eff}}$  and  $\log g$ . The median difference in metallicity for solar-type stars is smaller than for the coldest, hottest and metal-poor stars. The differences obtained are usually related to larger deviations in  $T_{\text{eff}}$  and  $\log g$  from the fundamental value, as seen in Fig. 9 and also discussed in e.g. Allende Prieto et al. (2004) and Ramírez & Allende Prieto (2011). In Gmb 1830, for example, the results of  $T_{\text{eff}}$  and  $\log g$  from the free spectral analysis agree better with what has been reported in PASTEL (Soubiran et al. 2010), which is more than 250 K above the fundamental value. HD140283 is another case where free temperature and surface gravity are 200 K and 0.7 dex smaller than the fundamental value, resulting in a  $[\text{Fe}/\text{H}]$  that is  $\sim 0.2$  dex more metal-poor than the fixed case. On the other hand, the smallest differences in  $[\text{Fe}/\text{H}]$  are related to small deviations in  $T_{\text{eff}}$  and  $\log g$ . Examples of this cases are  $\mu$  Cas A,  $\alpha$  Cen A,  $\alpha$  Cen B and the Sun.

In general, when looking at the results of individual methods, a difference of at least 200 K in  $T_{\text{eff}}$  and 0.25 dex in  $\log g$  would be necessary to restore excitation and ionization balance in the problematic benchmark stars. This would introduce a change of  $\sim 0.1$  dex in metallicity as well. It is important to comment that this test is just an illustration of freeing  $T_{\text{eff}}$  and  $\log g$  to retrieve ionization balance but does not represent the real performance on the different methods when determining three parameters per se, since here we are only concentrating in the analysis of iron lines and not other important spectral features that can affect the determination of  $T_{\text{eff}}$  and  $\log g$ . This can have important consequences in methods based on the SME or the MATISSE program, for example.

### 5.5. N-LTE corrections

Recently, Bergemann et al. (2012) presented a thorough investigation of the Fe I-Fe II ionization balance in five of the benchmark stars included here (Sun, Procyon, HD122563, HD84937, HD140283) and one more extremely metal-poor star (G64-12). In particular, they utilized an extensive model atom and both traditional 1D and spatially and temporally averaged 3D hydrodynamical models to assess the magnitude of NLTE effects on Fe line formation. Bergemann et al. (2012) concluded that only very minor NLTE effects are needed to establish ionization balance at solar metallicities, while very metal-poor stars imply effects on the order of +0.1 dex on Fe I lines. Fe II lines are everywhere well modeled by the LTE assumption.

The NLTE calculations were extended by Lind et al. (2012) to cover a large cool star parameter space. Here, we have interpolated in the grid of NLTE corrections by Lind et al. (2012) to the stellar parameters adopted for each benchmark star as taken from Paper I and Tab. 1. Each Fe line used in the final  $[\text{Fe}/\text{H}]$  determination was corrected individually. When a NLTE correction was not available for a specific line, we used the median of the corrections computed for all other lines. The difference between the final Fe abundances for single and ionized lines is visualized in Fig. 10 for each star (see Sect. 6 for details of how the final abundances are determined). The stars are plotted in increasing order of effective temperature. Black indicates that

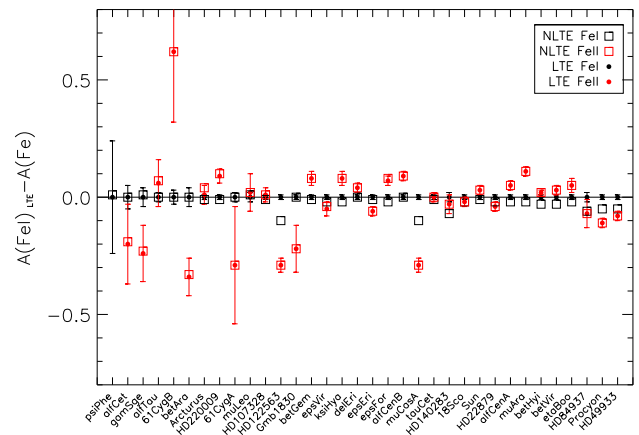


**Fig. 10.** Difference of final Fe I (black) and Fe II (red) for each benchmark star. Squares show the abundances after NLTE corrections.

the iron abundance is determined from Fe I lines while red indicates that the abundance is determined from Fe II lines. Dots and square symbols indicate the LTE and NLTE abundances, respectively. The errors bars for the abundances (see also Sect. 6 for details of error estimation) are plotted only for the LTE abundances, as it does not change after NLTE corrections.

In general, NLTE corrections can vary between -0.10 to +0.15 dex for individual lines, but on average the departures of NLTE affect the metallicity by  $<0.05$  dex for all stars, except the hottest stars and the most metal-poor ones, which can differ up to 0.1 dex. Since the corrections due to NLTE effects are small, even when looking at the final NLTE abundances in Fig. 10, we still find cases where ionization imbalance is significant, especially for the cold stars. We conclude that neglecting NLTE effects is not a likely explanation for the ionization imbalance.

## 6. The metallicity and its uncertainty

Since each method and corresponding criterium used to give a final  $[\text{Fe}/\text{H}]$  value differ, we combine our results by looking at individual abundances in a line-by-line approach. Since the Nice method is based on a global fitting of a whole section of the spectrum, abundances of individual lines for that method are not provided. We comment that the setup employed by the LUMBA node for this analysis performed a simultaneous fit of all pixels contained in the specified line mask, and thus it did not provide abundances of individual lines per se. However, LUMBA employed a post-processing code, which determined best-fit  $\log gf$  values for each line. This is equivalent to determining best-fit abundances. The resulting  $\log gf$  deviation from the nominal value is then added to the global metallicity of each star derived by SME in order to reconstruct individual line abundances. Figure 11 shows four examples of how the different nodes compare to each other at a line-by-line basis. Looking the result in this way does not show any node as being particularly different to the others, as many of the individual abundances agree. We also do not see any node presenting a significantly higher internal scatter than the rest.

We performed several steps to combine and thus determine the metallicity of each star. This analysis was mostly carried out by P. Jofré, U. Heiter, J. Sobeck and K. Lind.

Firstly, we selected those lines with  $\log(\text{EW}/\lambda) \leq -4.8$ . The objective was to use lines which are on the linear part of

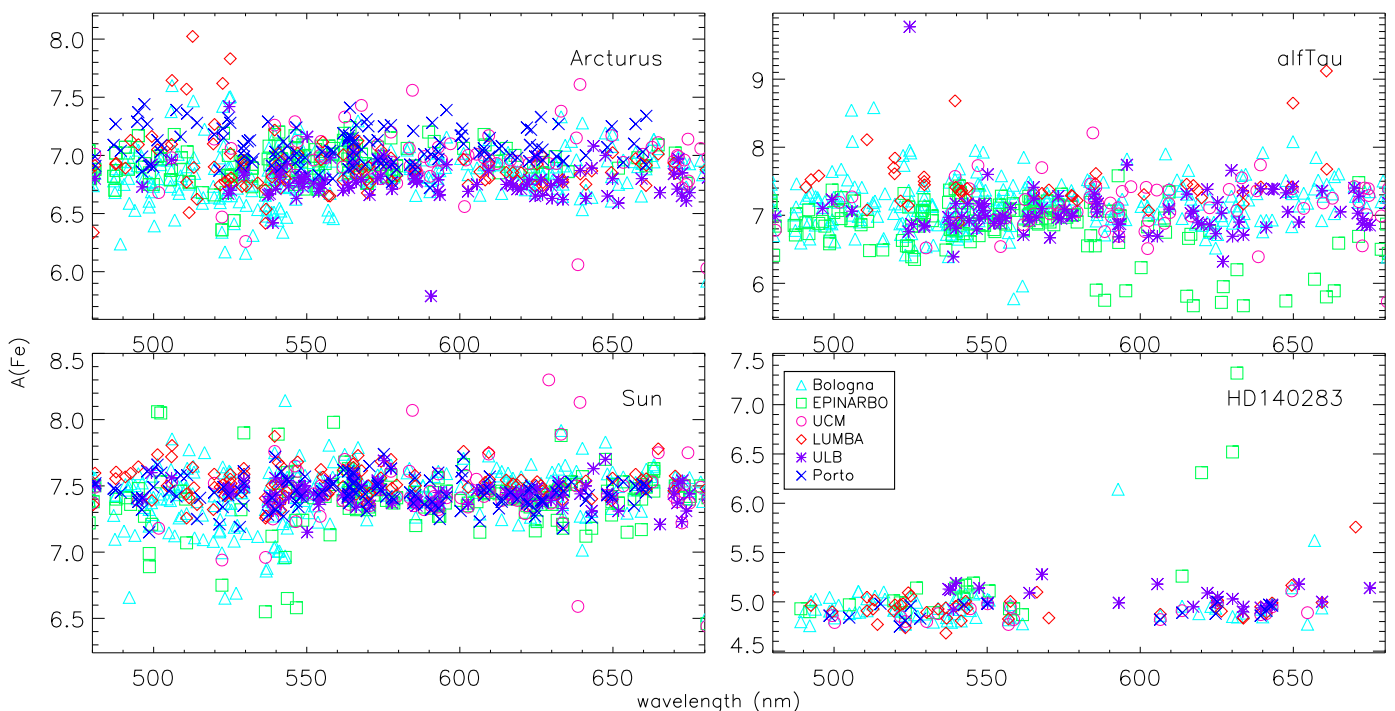


**Fig. 11.** Example of abundances of individual lines of four benchmark stars. Each symbol represent a different method.

the curve of growth, in order to avoid saturated lines and mitigate the effect of “wrong microturbulence” and “wrong damping parameters” which affect strong lines. The transition from the linear part to the saturated part of the curve of growth occur at  $\log(EW/\lambda) \sim -5.0$ , more or less independent of stellar parameters (See e.g. Figs. 16.1 to 16.6 of Gray 2005, or Villada & Rossi 1987). The transition point is slightly above -5 for cold models, while slightly below -5 for hot models. In addition, the transition value was checked for each benchmark star by constructing empirical curves of growth from the output of the Bologna method. For the different kind of stars presented here, the limit of -4.8 seems to be a good compromise between the number of lines and the saturation criterion.

Secondly, we calculated the mean and standard deviation of the total abundances and selected those lines that were analyzed by at least three different groups and that their values agreed within two  $\sigma$  of the standard deviation.

Thirdly, we calculated the mean abundance for each selected line. For consistency checks on metallicities, each abundance was plotted as a function of wavelength, EW and excitation potential (E.P.) to account for excitation balance. The relations can be found in Fig. 12, 13, 14, 15 and 16. Additionally, NLTE corrections were applied individually for each selected line and star (see Sect. 5.5). An extensive discussion is found in Sect. 6.2

Finally, we computed the final value of Fe I and Fe II abundances from the average of the selected lines. To compute the final metallicity, we have considered the value of  $A(\text{Fe}) = 7.45$  for the solar iron abundances from Asplund et al. (2009). The final results can be found in Tab. 3. Uncertainties correspond to the standard deviation of the mean and to the errors associated to the other stellar parameters, namely  $T_{\text{eff}}$ ,  $\log g$  and  $v_{\text{mic}}$  (see below)

### 6.1. Errors due to uncertainties in $T_{\text{eff}}$ , $\log g$ and $v_{\text{mic}}$

We are basing our analysis on fixed values for  $T_{\text{eff}}$  and  $\log g$ , but these values have associated errors that give the metallicity an

additional uncertainty. In a similar manner, we want to study the effect of the final metallicity due to the uncertainties in the  $v_{\text{mic}}$  parameter. To quantify the error of  $[\text{Fe}/\text{H}]$  due to the associated errors in  $T_{\text{eff}}$ ,  $\log g$  and  $v_{\text{mic}}$ , we have performed additional runs by determining the iron abundances using the same setup as described for *run-nodes* in Sect. 4, but changing the input value of  $T_{\text{eff}}$ ,  $\log g$  and  $v_{\text{mic}}$  by considering  $T_{\text{eff}} \pm \Delta T_{\text{eff}}$ ,  $\log g \pm \Delta \log g$  and  $v_{\text{mic}} \pm \Delta v_{\text{mic}}$ , respectively. The values of  $\Delta T_{\text{eff}}$  and  $\Delta \log g$  can be found in Paper I, while for the value of  $\Delta v_{\text{mic}}$  we considered the scatter found by the different nodes from the standard *run-nodes* (see also Fig. 4).

This analysis gave us 6 additional runs, which were performed by the methods LUMBA, EPINARBO, Porto, UBL and UCM. To be consistent with our main results, we determined the iron abundance of only the lines that passed the selection criteria after the main run. The final differences of  $([\text{Fe}/\text{H}]_{\Delta^-} - [\text{Fe}/\text{H}]_{\Delta^+})$ , where  $[\text{Fe}/\text{H}]_{\Delta^\pm}$  correspond to the metallicities obtained considering the parameters  $\pm$  their errors, for  $T_{\text{eff}}$ ,  $\log g$  and  $v_{\text{mic}}$  respectively, were conservatively added quadratically based on standard propagation of errors. These values are also listed in Tab. 3 for each star, where the number of selected lines of Fe I and Fe II are also indicated for each star.

## 6.2. Discussion

To understand better our results, we have divided the stars into 5 groups: metal-poor stars, FG dwarfs, FGK giants, M giants, and K dwarfs. Each group is discussed separately in the following sections.

### 6.2.1. Metal-poor stars

This group includes the stars HD122563, HD140283 and HD84937. Our results agree well with an internal scatter at a line-by-line approach of about 0.12 dex before the line selection process described in Sect. 6. A similar differential analysis between the results obtained for atmospheric parameters from

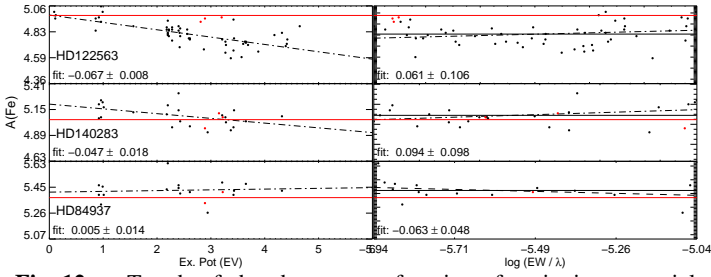


**Fig. 12.** Trends of abundances as a function of excitation potential (left panels) and reduced equivalent width (right panels) in the group of metal-poor stars (Similar to Figs. 13, 14, 15 and 16)

equivalent widths and synthetic spectra on high resolution spectra of metal-poor stars was done by Jofré et al. (2010). In that study, 35 turn-off metal-poor stars were analyzed using the same data and line list and different atmosphere models. The general scatter was 0.13 dex in metallicity when  $\log g$  and  $T_{\text{eff}}$  were forced to agree by 0.1 dex and 100 K, respectively. Although here we determine only metallicity, it is encouraging to obtain a mean scatter of 0.06 dex when considering the independent results of the 7 methods.

The abundances of the selected lines for each metal-poor star as a function of E.P. are shown in the left panels of Fig. 12, while the abundances as a function of reduced EW are shown in the right panels of the figure. Black dots correspond to Fe I abundances, corrected by NLTE effects as described in Sect. 5.5, while the red dots correspond to the Fe II abundances. The solid red and black horizontal lines indicate the averaged Fe II and Fe I abundance, respectively. In addition, we have plotted with a dot-dashed line the regression fit of the Fe I abundances, where its slope and error are written in the bottom of each panel.

In metal-poor stars the continuum is easy to identify, although other difficulties appear, such as the low number of iron lines detectable in the spectra, especially those of ionized iron. In our case, the common lines that passed the selection criteria explained above can be seen in Fig. 12. HD84937 is the most extreme case, where we have only 3 ionized and 17 neutral iron lines that are used for the final  $[\text{Fe}/\text{H}]$  determination.

NLTE effects can change significantly the metallicity of metal-poor stars (Thévenin & Idiart 1999; Asplund 2005). The results listed in Tab. 2 consider LTE, therefore explaining the differences between individual results and the literature as listed in Tab. 1 and in Fig. 3. After applying NLTE corrections to our selected LTE Fe I abundances, the metallicities increase by up to approximately 0.1 dex, which agree with the investigation of Bergemann et al. (2012) for these three benchmark stars.

The largest difference between Fe I and Fe II abundances is for the metal-poor giant HD122563. When looking at the distribution of Fe I lines as a function of E.P. one can see a significant slope in the regression fit of  $-0.067 \pm 0.008$ . The regression fit as a function of EW shows a slope of 0.061 that can be neglected when considering the error of 0.106. Since those fits are obtained after making the NLTE corrections, we attribute this trend to 3D effects, which are most important for cool metal-poor stars (Asplund et al. 1999; Collet et al. 2007, e.g.). See also Bergemann et al. (2012) for the study in this regard of HD122563. The second metal-poor star, HD140283 also presents a negative slope for Fe I abundances as a function of E.P., although it is less pronounced and the error of it is larger than the case of HD122563. It is interesting to see that for this metal-poor subgiant we obtain a good ionization balance. The last metal-poor star of our group, HD84937, presents a quite flat

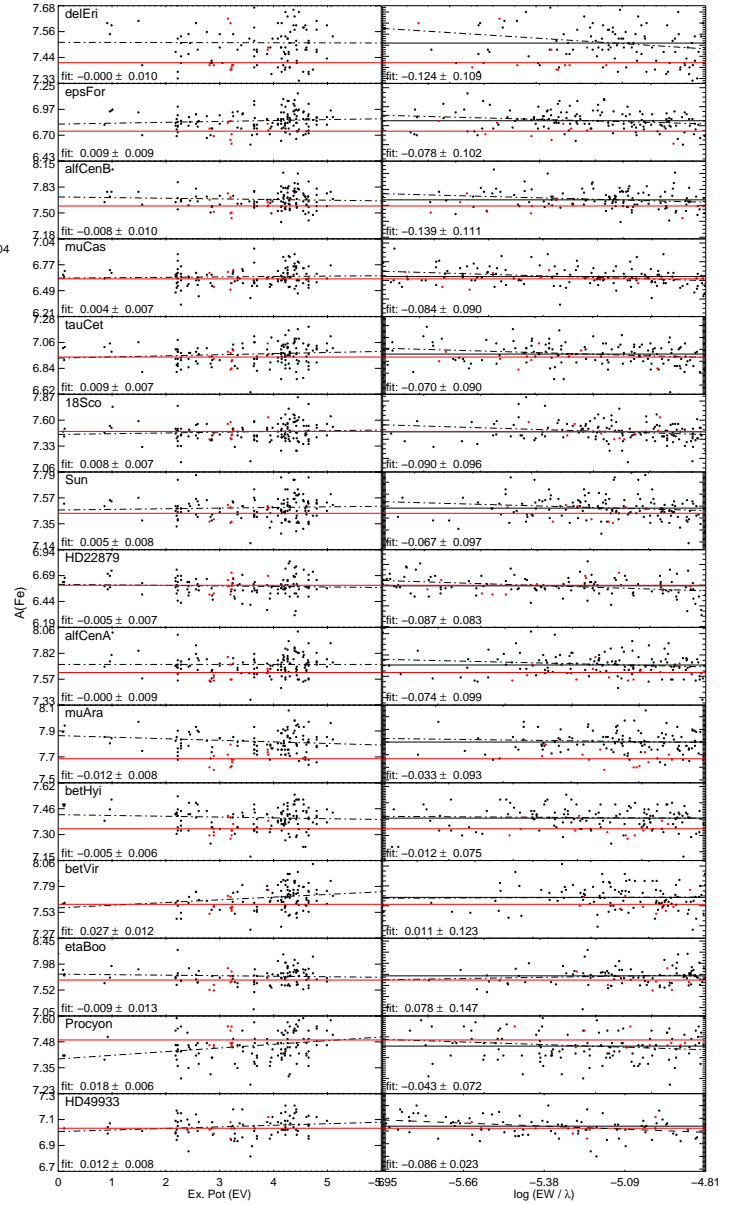


**Fig. 13.** Trends for group of FG dwarfs. Similar to Figs. 12, 14, 15 and 16

regression fit when looking at the abundances as a function of E.P or EW and considering the errors. Moreover, Fe I and Fe II abundances agree better when the errors due to  $T_{\text{eff}}$  and  $\log g$  are taken into account.

We conclude that although one should be aware that there is a large ionization and excitation imbalance for HD122563, we can average the abundances and obtain robust values of metallicities for metal-poor stars given their fundamental parameters and associated errors.

## 6.2.2. FG dwarfs

The stars  $\delta$  Eri,  $\epsilon$  For,  $\alpha$  Cen A & B,  $\mu$  Cas,  $\tau$  Cet, 18 Sco, Sun, HD22879,  $\mu$  Ara,  $\beta$  Hyi,  $\beta$  Vir,  $\eta$  Boo, Procyon and HD49933 belong to this group. The mean internal  $1\sigma$  scatter of these stars when looking at all abundances of individual lines is of 0.13 dex, while the value when looking at the results of the individual methods is of 0.07 dex. Moreover, our results agree

**Table 3.** Final metallicity of benchmark stars obtained via combination of individual line abundances. Three values of metallicity are provided, considering abundances taken from Fe I lines, Fe II lines and Fe I lines after the corresponding NLTE corrections, which are indicated in the first three columns, respectively. The fourth and fifth columns list the  $1\sigma$  scatter of the abundances of Fe I and Fe II, while the sixth and seventh columns list the uncertainty of metallicity of Fe I and Fe II due to the associated errors in  $T_{\text{eff}}$ ,  $\log g$ , and  $v_{\text{mic}}$ . The last two columns indicate the number of selected lines used for the determination of Fe I and Fe II abundances.

star	[Fe I/H]	[Fe II/H]	[Fe <sub>NLTE</sub> /H]	$\sigma$ Fe I	$\sigma$ Fe II	$\Delta$ [Fe I/H]	$\Delta$ [Fe II/H]	N Fe I	N Fe II
<b>Metal-Poor</b>									
HD122563	-2.74	-2.47	-2.64	0.01	0.03	0.03	0.04	55	4
HD140283	-2.43	-2.40	-2.36	0.02	0.04	0.01	0.05	23	2
HD84937	-2.09	-2.08	-2.03	0.02	–	0.01	–	17	1
<b>FG dwarfs</b>									
$\delta$ Eri	0.06	0.03	0.06	0.01	0.02	0.01	0.04	119	11
$\epsilon$ For	-0.62	-0.71	-0.60	0.01	0.02	0.03	0.02	139	8
$\alpha$ Cen B	0.22	0.14	0.22	0.01	0.02	0.00	0.03	121	9
$\mu$ Cas	-0.82	-0.83	-0.81	0.01	0.02	0.02	0.01	129	7
$\tau$ Cet	-0.50	-0.51	-0.49	0.01	0.02	0.03	0.01	136	10
18 Sco	0.01	0.03	0.03	0.01	0.02	0.02	0.01	136	10
Sun	0.02	-0.01	0.03	0.01	0.02	0.02	0.01	140	9
HD22879	-0.88	-0.85	-0.86	0.01	0.02	0.01	0.01	114	10
$\alpha$ Cen A	0.24	0.19	0.26	0.01	0.02	0.02	0.02	130	12
$\mu$ Ara	0.33	0.22	0.35	0.01	0.02	0.02	0.02	119	13
$\beta$ Hyi	-0.07	-0.11	-0.04	0.01	0.01	0.01	0.01	128	12
$\beta$ Vir	0.21	0.17	0.24	0.01	0.02	0.01	0.01	108	10
$\eta$ Boo	0.30	0.27	0.32	0.01	0.03	0.01	0.02	100	10
Procyon	-0.04	0.04	0.01	0.01	0.02	0.03	0.01	122	12
HD49933	-0.46	-0.43	-0.41	0.01	0.02	0.01	0.03	90	6
<b>FGK giants</b>									
Arcturus	-0.53	-0.56	-0.52	0.01	0.04	0.12	0.10	105	10
HD220009	-0.75	-0.86	-0.74	0.01	0.03	0.12	0.07	111	11
$\mu$ Leo	0.26	0.23	0.25	0.02	0.08	0.24	0.29	83	11
HD107328	-0.34	-0.32	-0.33	0.01	0.03	0.27	0.23	93	11
$\beta$ Gem	0.12	0.04	0.13	0.01	0.03	0.25	0.20	101	13
$\epsilon$ Vir	0.13	0.17	0.15	0.01	0.03	0.28	0.28	90	12
$\xi$ Hya	0.14	0.07	0.16	0.01	0.03	0.33	0.29	111	11
<b>M giants</b>									
$\psi$ Phe	-1.23	–	-1.24	–	–	0.56	–	17	1
$\alpha$ Cet	-0.45	-0.33	-0.45	0.05	0.17	0.55	0.35	27	3
$\gamma$ Sge	-0.16	0.08	-0.17	0.04	0.12	0.51	0.31	20	4
$\alpha$ Tau	-0.37	-0.43	-0.37	0.02	0.10	0.25	0.24	55	9
$\beta$ Ara	-0.05	0.37	-0.05	0.04	0.08	0.39	0.46	35	8
<b>K dwarfs</b>									
61 Cyg B	-0.38	–	-0.38	0.03	–	0.01	–	98	1
61 Cyg A	-0.33	-0.04	-0.33	0.02	0.25	0.00	0.08	113	3
Gmb 1830	-1.46	-1.24	-1.46	0.01	0.10	0.01	0.06	99	4
$\epsilon$ Eri	-0.10	-0.04	-0.09	0.01	0.02	0.00	0.02	114	11

within 0.04 dex with the literature, as seen in Fig. 3. Note that the final line-to-line scatter for these stars is reduced to  $\sim 0.01$  from the original one after our selection of lines. NLTE corrections for these stars are very small, usually less than 0.03 dex, with exception of Procyon and HD49933, which are of the order of 0.05 dex (see Fig. 10). These stars have high effective temperatures, which produce greater departures from LTE than cold stars (Bergemann et al. 2012).

As in the case of the metal-poor group, we have plotted the abundances of the selected lines for each star as a function of E.P. and reduced EW in Fig. 13. This group shows that our selected lines are well-behaved, in the sense that excitation and ionization balance are in general satisfied. Usually a difference between ionized and neutral iron abundances is less than 0.1 dex for this group of stars, which can be confirmed with Fig. 10. There are few exceptions, such as the hot stars Procyon and HD 49933,

and the solar-type stars  $\epsilon$  For,  $\alpha$  Cen B and  $\mu$  Ara. The latter presents the larger ionization imbalance, which can be explained by the rather large excitation imbalance (with a slope of  $-0.012 \pm 0.008$  dex in the regression fit as a function of E.P.). We find no significant trend as a function of  $\log(\text{EW}/\lambda)$  when considering the errors of the regression fits. Note that the hot stars Procyon and HD49933 also present a significant excitation imbalance in the regression fits.

Recently, Torres et al. (2012) made a comparative spectral analysis of FG dwarfs using three different methods to determine parameters. Two of their methods overlap with our own, namely SME (LUMBA) and MOOG (UCM, Porto and EPINARBO). They obtained a systematic difference of  $0.068 \pm 0.14$  dex in metallicity when analyzing 31 stars with these two methods, which is attributed to the different  $T_{\text{eff}}$  and  $\log g$  obtained from the simultaneous analysis, the different way of placing the con-

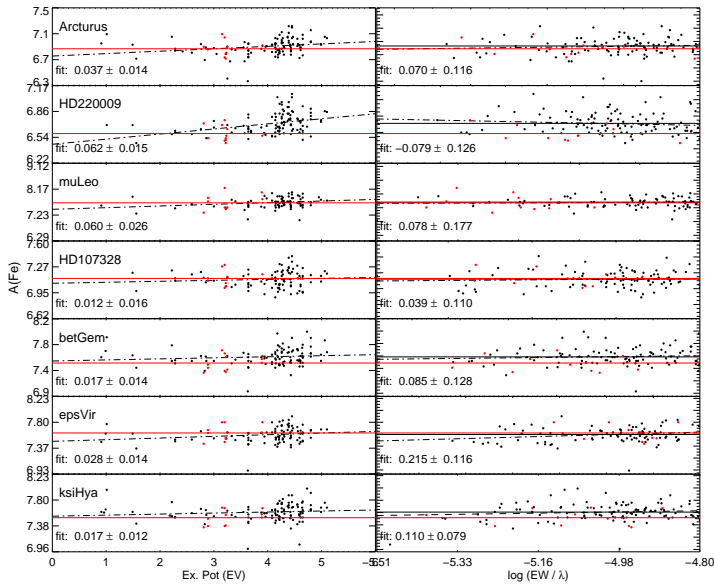


**Fig. 14.** Trends for group of FGK giants. Similar to Figs. 12, 13, 15 and 16

tinuum, and the different lines used by each methods. Here we can see the improvement in the agreement in  $[\text{Fe}/\text{H}]$  between our methods when determining only one parameter and constraining our line list.

We conclude that it is acceptable to average the abundances of our selected lines and that we are able to provide robust results for  $[\text{Fe}/\text{H}]$  for FG dwarfs based on their fundamental temperature and surface gravity.

### 6.2.3. FGK giants

They are Arcturus,  $\mu$  Leo,  $\beta$  Gem,  $\epsilon$  Vir,  $\xi$  Hya, HD220009 and HD107328. Although the scatter between the nodes is larger than the scatter for dwarfs (see Fig. 3), it is encouraging to obtain an agreement within 0.08 dex for giants considering the different methods. The mean  $1\sigma$  scatter of all iron abundances for every line is of 0.2 dex, although it is reduced to 0.08 dex when considering only the abundances of the selected lines. FGK giants are challenging objects to model due to their complex atmospheres and large number of lines, in particular lines that formed by molecules. In addition, convection in red giants becomes important and 1D models can differ from 3D models, impacting the final abundances, especially for metal-poor stars (Collet et al. 2007). Microturbulence becomes therefore a sensitive parameter, which explains the different  $v_{\text{mic}}$  results in Fig. 4.

Typically NLTE departures for this group of stars is negligible when compared with the errors obtained for the abundances, which can be seen in Fig. 10. In general, ionization imbalance of  $\sim 0.1$  dex is found for this group of stars, which agrees with the recent conclusion of Ramirez & Allende Prieto (2011). The abundances of the selected neutral and ionized iron lines for each giant are shown in Fig. 14. Like in Fig. 12 and 13, black and red dots indicate the abundances of Fe I and Fe II respectively, with their mean represented by the horizontal line. The dot-dashed lines correspond to the linear regression fits of the Fe I abundances as a function of E.P and  $\log(\text{EW}/\lambda)$ . While for most of the stars no significant trend of abundances as a function of reduced EW is obtained when considering the error of the fit, a significant positive slope in the regression fit as a function of E.P. is found. The error of the slope is, however, smaller than the

final error in  $[\text{Fe}/\text{H}]$  when considering the uncertainties in the stellar parameters.

Since in most of the stars the scatter of the fit is larger than the slope by usually more than one order of magnitude, we are confident that performing a mean on the abundances of our selected lines provides robust results for the  $[\text{Fe}/\text{H}]$  of the benchmark FGK giants.

We obtain typical differences of about  $\pm 0.07$  dex or less with the literature values, which is within the uncertainties and scatter found by us and by the literature. As exceptional cases, we obtain a slightly lower metallicity of 0.1 dex than the literature value for  $\xi$  Hya. The PASTEL catalogue has only two works reporting parameters for this star, where McWilliam (1990) obtained  $[\text{Fe}/\text{H}] = -0.04$  while Bruntt et al. (2010) obtained  $[\text{Fe}/\text{H}] = +0.23$ . In Tab. 1 we present only the latter one due to the restriction on publication year for the extraction from PASTEL (see Sect. 2). Our value of  $[\text{Fe}/\text{H}] = 0.12$  lies in between those values. Also, for HD220009 we obtain  $\sim 0.14$  dex lower than the literature. The only work in PASTEL after 2000 that reports  $[\text{Fe}/\text{H}] = -0.67$  is that of Smiljanic et al. (2007). The difference can be explained from the different values for the stellar parameters considered by that work, i.e. effective temperature and surface gravity 100 K and 0.5 dex, respectively, higher than the fundamental values considered by us.

Finally we comment that during the time when this analysis was carried out by our different groups, we noticed that the effective temperature of HD107328 was overestimated by 90 K. For that reason, we created a set of line-by-line corrections for HD107328 to account for the lower temperature. We used the same grid as for the NLTE corrections, but using only LTE curves-of-growth. The uncertainties in the metallicity due to associated errors in the other stellar parameters were then determined using the latest temperature.

### 6.2.4. M giants

The analysis of this group is the most difficult one, where an averaged line-to-line scatter of 0.5 dex is obtained. It includes the stars  $\psi$  Phe,  $\alpha$  Cet,  $\beta$  Ara,  $\gamma$  Sge,  $\alpha$  Tau. Note that the spectral class  $\alpha$  Tau is not well established (see Lebzelter et al. 2012, for a discussion), being in the limit between late K and early M type. Since our results for  $\alpha$  Tau are more comparable to those of the M- than those of FGK group of giants, for simplicity, we classify  $\alpha$  Tau into the M giant group.

These cold giants have very challenging spectra, mostly of because of the presence of molecules. The strength of TiO and CN absorption bands in the coldest stars is particularly high (Peterson 1976), making it extremely difficult to identify the continuum around most of the iron lines. The blends with molecules can become so dominating that an overestimation of metallicity can be obtained when using a given line which has an unidentified molecular blend (Peterson 1976).

Additionally, the efficiency of convective energy transport and its effect on line-formation reaches its maximum at  $T_{\text{eff}} \sim 4000$  K (Heiter et al. 2002). For that reason 3D hydrodynamical models are much more suitable for modeling line-formation in such spectra. Such models for stars other than the Sun are not easily available, mainly due to the large computing power needed to process them. In particular, red supergiants give rise to large granules that can imprint irregular patterns (Chiavassa et al. 2009, 2010), but the influence of this effect in spectra of such cool stars has not been investigated so far. A detailed discussion on spectral modeling for cold giants can be found in Lebzelter et al. (2012). They determined atmospheric

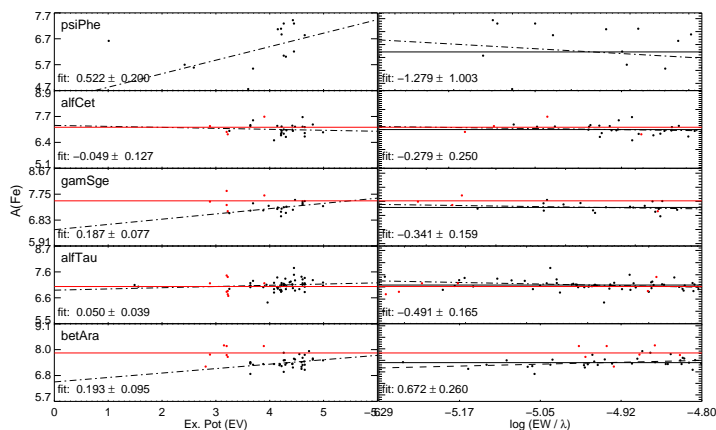


**Fig. 15.** Trends for group of M giants. Similar to Figs. 12, 13, 14 and 16

parameters of the benchmark stars  $\alpha$  Cet and  $\alpha$  Tau using 11 different methods and made a comparative analysis like this work. In their analysis (employing also different linelists and atmosphere models between the methods) the unweighted mean values for metallicity were  $[\text{Fe}/\text{H}] = -0.2 \pm 0.2$  dex for both stars. We obtain a value of  $-0.45$  for  $\alpha$  Cet and  $-0.37$  for  $\alpha$  Tau, respectively. Although we obtain values that are more metal-poor, they lie within the errors.

The abundances of the selected lines can be visualized in Fig. 15. Because of the reasons explained above, we obtain few un-blended and clean lines that pass our selection criteria for which the different methods that pass our selection criteria. In this work,  $\alpha$  Tau and  $\alpha$  Cet show a good ionization and excitation balance, although the scatter of the regression fit, as well as the uncertainties of our results are quite high. The other three stars of this group show, on the other hand, a significant slope of the regression fit as a function of E.P. Note, however, we have no lines at low excitation potentials, making the regression fit not a good representation of real trend. We obtain also significantly high slopes in the regression fit as a function of reduced EW, even when considering the large errors obtained in the fits.

In a similar manner than for the case of FGK giants, the final errors obtained for the iron abundances when considering the uncertainties in the stellar parameters are larger than the slope of the regression fit and its error.

NLTE effects are very small compared with the uncertainties obtained for the abundances. Ionization balance is, on the other side, unsatisfied for this group except  $\alpha$  Tau and  $\alpha$  Cet, when considering the errors. The most extreme case are  $\psi$  Phe and  $\beta$  Ara. As discussed in Sect. 5.4, it is impossible to find enough clean and unblended Fe II lines in this wavelength domain for such low temperatures, making our Fe II results thus unrealistic. We can see for example in the panel of  $\psi$  Phe that the Fe II abundances obtained correspond to a value  $> +0.5$  dex (2 dex), which is unphysical.

It is important to comment further on  $\psi$  Phe and  $\beta$  Ara. We have found only one old reference for metallicity in the PASTEL catalogue for  $\beta$  Ara (Luck 1979). Being aware of the difficulties in the analysis of these stars, we expect the Fe I abundances obtained by us to be uncertain, but finally only one of our methods (Porto) could not provide a final value. Given this, we find it encouraging to obtain a scatter between our methods of only 0.22 and 0.17 dex, a line-to-line scatter of 0.24 and 0.04 dex and an uncertainty of 0.56 and 0.39 dex due to stellar parameter errors, for  $\psi$  Phe and  $\beta$  Ara, respectively.

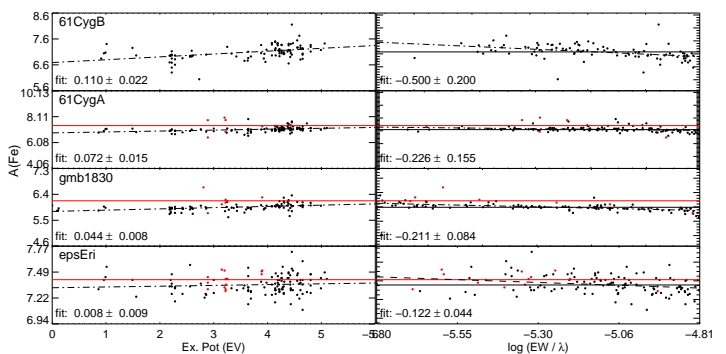


**Fig. 16.** Trends for group of K dwarfs. Similar to Figs. 12, 13, 14 and 15

### 6.2.5. K dwarfs

Gmb 1830, 61 Cyg A, 61 Cyg B and  $\epsilon$  Eri are the benchmark K dwarfs. As in the previous groups, we have plotted in Fig. 16 the abundances of the selected lines for each star in different panels. Even after considering the errors, this group does not present a good excitation balance, since significant trends are obtained for the regression fits for both E.P. and EW. The most extreme case is 61 Cyg B, where the Fe I abundances increase as a function of E.P. at a rate of  $0.11 \pm 0.02$  and decrease as a function of reduced EW at a rate of  $0.5 \pm 0.2$ . This star is very cold, and therefore its spectrum is very affected by blends of molecules that are not considered in our line list. A more suitable line list for such cold stars might help in obtaining a better excitation balance. This star also presents the largest ionization imbalance, which might be related to the difficulty in obtaining realistic Fe II abundances due to the strong blends of molecules present for most of the ionized iron lines of this spectrum (for a discussion on this issue see the previous section and also Luck & Heiter 2005)

Note that 61 Cyg A and 61 Cyg B belong to a binary system, expecting therefore the same metallicity for both stars. We obtain a value of  $-0.33$  dex and  $-0.38$  dex for the A and B components, respectively. The difference of 0.05 dex is within the errors. These values are about 0.15 dex lower than the literature values. We attribute this difference by the different temperature adopted by, e.g. Luck & Heiter (2005), of 4640 K and 4400 K for the components A and B, respectively. These temperatures are  $\sim 300$  K above the values adopted by this work.

It is worth mentioning that during one of the first attempts to determine metallicities for this system, the values of fundamental  $\log g$  considered for the analysis were different (4.49 and 4.61 dex) because they were obtained from evolutionary tracks of  $[\text{Fe}/\text{H}] = -0.10$  and  $[\text{Fe}/\text{H}] = -0.30$ , for the A and B components of 61 Cyg, respectively. At that time, we retrieved a new metallicity of  $-0.49$  and  $-0.55$  dex for 61 Cyg A and B, respectively, which was translated to a difference in  $\log g$  of  $-0.06$  and  $-0.08$ , respectively. A third iteration on  $\log g$  with the newest metallicity, and a further iteration on  $[\text{Fe}/\text{H}]$  with the newest surface gravity would be desirable, although we have decided not to do to this because of the large errors associated with the mass of this system (see Paper I) and also the errors obtained here for the final  $[\text{Fe}/\text{H}]$ .

Note that the metallicity obtained for Gmb 1830 differs from the literature by  $\sim 0.12$  dex. The 19 works after 2000 in PASTEL have a mean temperature of  $5090 \pm 89$  K, which is more than 250 K above the fundamental value. Recently, Creevey et al. (2012), who determine the temperature chosen for Paper I, obtain a value that is about 200 K less than the classical values obtained from the PASTEL catalogue. They suggest a revision of the metal-

licity based on this fundamental value. We have done this here and we have seen that the consequence is a considerable ionization and excitation imbalance for this new temperature. We have also studied the NTLE effects and concluded that they are not significant in this particular star. Moreover, Gmb 1830 is not so cold as to be strongly affected by molecules, however, its rather low metallicity and mass ( $0.6 M_{\odot}$ ) suggests 3D or granulation effects caused by convection. The trends found in Fig. 16 and the ionization imbalance could be partly explained by the use of inaccurate 1D LTE models, but we can not exclude the possibility that the fundamental temperature might be too low or perhaps there is another effect that has not been investigated so far, such as magnetic fields or other activity process in the atmosphere. We noted that the knee in the curve of growth of this star is earlier than other stars, which could lead to an underestimate of the strong lines by the EW methods and this could bias the  $v_{\text{mic}}$  measurement and also other slopes in this analysis, although not that significant as that seen here.

### 6.3. Line list: Golden lines

In this section, we give an overview of the Fe I and Fe II line selection and line data which have been used to derive the final metallicity values listed in Tab. 3. Only the lines which remained after the selection process described in Sect. 6 were considered. We determined which lines were used in common for each of the groups defined in Section 6.2 and refer these as the “golden lines”. We found that there were significant differences in line selection between individual methods within several star groups, and thus the group definitions were somewhat expanded as explained below. The unique lists of 171 Fe I and 13 Fe II lines occurring in any of the groups can be found in Tables 4 and 5, respectively. The tables give the most relevant atomic data. For the lines identified for each individual group, we give the minimum and maximum standard deviations of the average line abundances, and the minimum and maximum number of abundances averaged for each line in the respective column.

The *metal-poor stars* (Sect. 6.2.1) were divided into dwarfs (HD 84937, HD 140283) and giants (HD 122563) and designated “MPD” and “MPG”, respectively, in Tables 4 and 5. As can be seen in the tables, the number of golden lines is considerably larger for the metal-poor giant (56 Fe I and 4 Fe II lines) than for metal-poor dwarfs (17 Fe I and 1 Fe II lines). 15 of the MPD Fe I lines are contained in the MPG list, while the single Fe II line common to the MPDs is different from the MPG Fe II lines. For the two MPDs, the standard deviations of the abundances are rather similar for all lines.

The group of *FG dwarfs* (Sect. 6.2.2) contains four stars for which the Fe I line selection differs from the others. This sub-group is designated “FGDb” in Tab. 4 and comprises  $\eta$  Boo, HD22879, HD49933, and Procyon. The remaining stars listed in Sect. 6.2.2 are designated “FGDa”. In general, the metallicity of the stars in the FGDb group is based on fewer Fe I lines than those in FGDa (see Tab. 3). However, the number of golden Fe I lines is similar for FGDa and FGDb (79 and 74, respectively), with 51 lines in common between the two sub-groups. The four stars in FGDb differ from those in FGDa in various respects, which reduce the number of useful lines: HD49933 and Procyon have the highest effective temperatures, HD49933 and  $\eta$  Boo have the largest  $v \sin i$ , and HD22879 is a moderately metal-poor star. The Fe II line lists are more homogeneous, resulting in six golden lines for all stars, with two exceptions as noted in Tab. 5 (column “FGD”). For the FG dwarfs, the abundance dispersions show a large variation from star to star. A more detailed inves-

tigation for the FGDa group shows that for Fe I lines the lowest minimum values are mostly due to the stars  $\beta$  Hyi, and the highest maximum values to  $\beta$  Vir. For most other stars and most Fe I lines the dispersion is around 0.06 dex. In the FGDb group, Procyon and HD22879 have the minimum dispersion for half of the Fe I lines each (and HD49933 for seven lines). The maximum dispersion is mostly due to  $\eta$  Boo (61 lines), and sometimes to HD49933 or Procyon (12 and 1 lines, respectively). The mode of the dispersion for FGDa is about 0.04 dex for all Fe II lines.

The group of *FGK giants* is comprised of the stars listed in Sect. 6.2.3. The 101 golden Fe I and 6 Fe II lines identified for this group are marked in column “FGKG” in Tables 4 and 5. For this group, the variation of dispersions is even larger than for FG dwarfs. The maximum dispersion for Fe I lines is mainly seen for  $\mu$  Leo (82 lines), while the minimum dispersion occurs mainly for HD220009, HD107328, and Arcturus (for 54, 16, and 12 lines respectively). For most other stars, the dispersion scatters around 0.08 dex. Also for the Fe II lines, the largest dispersion is found for  $\mu$  Leo. The dispersion is in general higher than for FG dwarfs (around 0.12 dex).

The group of *M giants* is comprised of the stars listed in Sect. 6.2.4, with one exception. The line list for  $\psi$  Phe differs significantly from the other stars (23 Fe I lines, of which only 6 are in common with the others). The 21 golden Fe I and 3 Fe II lines identified for this group are marked in column “MG” in Tables 4 and 5, while  $\psi$  Phe is listed in a separate column in Table 4 (no Fe II lines were selected for this star). The minimum abundance dispersion for Fe I lines in M giants is mostly found for  $\gamma$  Sge (13 lines), and the maximum dispersion equally often in  $\alpha$  Cet and  $\beta$  Ara (7 and 8 lines, respectively).  $\psi$  Phe shows in general high dispersions, with the notable exceptions of the Fe I lines at 6219.28 and 6336.82 Å, with dispersions of about 0.1 dex.

Finally, the group of *K dwarfs* described in Sect. 6.2.5 was divided into two sub-groups with two different lists of golden Fe I lines. These are designated “KDa” (61 Cyg A,  $\epsilon$  Eri) and “KDb” (61 Cyg B, Gmb 1830) in Table 4, with 127 and 85 Fe I lines, respectively, and 72 lines in common between the two sub-groups. The differences in line selection between the two sub-groups may be related to the specific parameter combinations ( $T_{\text{eff}}, [\text{Fe}/\text{H}]$ ) of the stars. In the KDa group, the maximum dispersion occurs for 61 Cyg A for 2/3 of the lines. In the KDb group, 61 Cyg B accounts for the maximum dispersion for most of the lines (77). Regarding the Fe II lines, the star  $\epsilon$  Eri stands out among the group members, with the largest number of lines selected (11 compared to 1–4). These are marked in Table 5 in column “KD”, which includes a note identifying the lines in common with the other three stars.

#### 6.3.1. Discrepant lines

It is important to discuss here that while selecting the golden lines, we could find that in some cases the derived abundances by our methods differed significantly, i.e. up to 0.4 dex even for FG dwarfs, for which we obtain the lowest line-to-line scatter in the final abundance determination (see above). This was surprising, since our golden lines were chosen to be unblended and are located in spectral regions with easy continuum placement. Moreover, our analysis is based on a great effort of having atomic data and model atmosphere homogeneous, making such differences difficult to explain.

Thus, we made a deep investigation of this issue and considered 4 examples of discrepant lines. This analysis was carried

out mainly by M. Bergemann, U. Heiter, P. Jofré, K. Lind, T. Masseron, J. Sobeck and H. Tabernero. We compared three of the involved radiative codes (SME, MOOG, Turbospectrum) and could see that their profiles were consistent when under consideration of the same stellar parameters. Naturally, a difference could still be seen due to different prescription and treatment of line and spectrum formation (collisional broadening, radiative broadening, scattering, limb darkening, spherical geometry, to name a few). But all together, this did not explain the 0.4 dex of the discrepant line examples.

We concluded that these discrepancies come apparently from a combination of different measured equivalent widths (differing up to 60%), the details of the fitting procedures, the choice of microturbulence parameter (see Fig. 4 for the different values) and the continuum placement. Understanding the contribution in the final discrepancy on each individual line from each of the aforementioned sources goes beyond the purpose of this paper. Here, we aim to combine abundances of numerous lines and methods homogeneously and provide a reference value for the metallicity of benchmark stars. In general, our results agree very well at a line-by-line basis and cases as those discussed here are rare, but we point out that this problem can arise even after performing analyses focused in homogeneity. Therefore, it is worth to investigate further the sources of these discrepancies.

## 7. Summary and Conclusions

We have made an extensive study on the determination of metallicity for the sample of 34 FGK benchmark stars introduced in Paper I. In this study we performed a spectral analysis of high SNR and high resolution ( $R \geq 70,000$ ) spectra taken from the library of benchmark stars described in Paper II. Two different libraries were analyzed, one with the spectra at its original resolution and the other one convolved to  $R = 70,000$ . In addition, the analysis was done for the same star observed with different instruments.

The analysis consisted of fixing effective temperature and surface gravity to the fundamental values presented in Paper I, and determining metallicity and microturbulence velocity simultaneously. Up to seven different methods were used for this analysis, all of them considering the same input material, such as spectra, line list and atmosphere models.

Three different runs were performed: *run-nodes*, consisting in the analysis of one spectrum per benchmark star, that allows a one-to-one comparison between different methods; *run-resolutions*, consisting in the analysis of the same spectrum of the previous run, but using this time its version in original resolution. This run allowed the study of the impact of the varied resolution. The third run, *run-instruments* consisted in the analysis of the whole library convolved to  $R = 70000$ , and allowed us to study instrumental effects. We obtained consistent and robust results, where the final metallicity was not biased either by method, resolution nor instrument.

Since we fixed  $T_{\text{eff}}$  and  $\log g$  by values that are independent of spectroscopy, the metallicity resulted in Fe I and Fe II abundances that did not necessarily agree. The comparison between neutral and ionized iron abundances was discussed, together with a quantification of how much  $T_{\text{eff}}$  and  $\log g$  would need to deviate from the fundamental value in order to comply with ionization balance, excitation balance and line strength balance. This was done by a test of determining  $T_{\text{eff}}$ ,  $\log g$  and  $v_{\text{mic}}$  together with [Fe/H].

To provide a final value of metallicity, we combined our results using a line-by-line approach. Starting from all individual

abundances of every method, we selected only those lines which were analyzed by at least three methods and agreed within  $2\sigma$  of the average of the total amount of lines. The selected lines were then averaged to have only one abundance per line, which was then used to perform NLTE corrections and quality checks such as ionization and excitation balance. We provide three metallicity values: (i) Fe I abundances, (ii) Fe II abundances, and (iii) Fe I abundances corrected by NLTE effects.

The errors were determined by considering the  $1\sigma$  scatter of the line-by-line analysis. In addition, we determined the uncertainty of the metallicity due to the errors associated with the effective temperature, surface gravity and microturbulent velocity. To do so, iron abundances were calculated by performing 6 additional runs only on the selected lines, each run fixing  $T_{\text{eff}}$ ,  $\log g$  and  $v_{\text{mic}}$  to the values considering their errors.

Generally, we were able to obtain robust values for [Fe/H] for all stars of our sample, making this work the first one to determine metallicity homogeneously for a complete set FGK benchmark stars. Our final [Fe/H] values are thus appropriate for use as reference values. When comparing our results with previous studies in the literature, we obtain a good agreement for 28 stars and different values for 5 stars (Gmb 1830, HD 220009, 61 Cyg A, 61 Cyg B,  $\beta$  Ara), which we adopt as a new reference [Fe/H]. In addition, we provide for the first time a value for the metallicity of  $\psi$  Phe. The final reference values and their uncertainty are indicated in Tab. 3.

Having well determined stellar parameters for the benchmark stars will improve the homogeneous analyses of current stellar surveys, which have become a key piece in Galactic studies. In addition, our extensive comparative study based on an homogeneous analysis of different spectral-type stars using different methods gives us a summary, in a general way, of different aspects of spectroscopy.

We have made a careful study in the selection of candidates to serve as benchmarks for stellar spectra analyses. The accurate distance and angular diameter of these stars provide us with fundamental determinations of effective temperature and surface gravity. Their closeness and brightness provide us with the possibility of having high quality spectra that suitable for an accurate determination of metallicity. This paper, together with Paper I and Paper II about benchmark stars, describe and discuss extensively our choice for the reference values of the three main stellar parameters  $T_{\text{eff}}$ ,  $\log g$  and [Fe/H] of FGK benchmark star. Using this material will allow for the connection of different methods and surveys, leading to a more consistent understanding of the structure and evolution of our Galaxy.

*Acknowledgements.* We thank all LUMBA members for the rich discussions on the development of SME for automatic analyses of spectra, which were crucial to the development of the setups used for the analysis of this project. P.J. acknowledges the useful comments and proof reading done by T. Madler. U.H. acknowledges support from the Swedish National Space Board (Rymdstyrelsen). S.G.S. acknowledges the support from the Fundaao para a Ciencia e Tecnologia (Portugal) in the form of the grants SFRH/BPD/47611/2008. The computations for the AMBRE project have been performed with the high-performance computing facility SIGAMM, hosted by OCA.

## References

- Adibekyan, V. Z., Figueira, P., Santos, N. C., et al. 2013, *A&A*, 554, A44
- Adibekyan, V. Z., Sousa, S. G., Santos, N. C., et al. 2012, *A&A*, 545, A32
- Allende Prieto, C., Barklem, P. S., Lambert, D. L., & Cunha, K. 2004, *A&A*, 420, 183
- Allende Prieto, C., Beers, T. C., Wilhelm, R., et al. 2006, *ApJ*, 636, 804
- Allende Prieto, C., Majewski, S. R., Schiavon, R., et al. 2008a, *Astronomische Nachrichten*, 329, 1018

- Allende Prieto, C., Sivarani, T., Beers, T. C., et al. 2008b, *AJ*, 136, 2070
- Alvarez, R. & Plez, B. 1998, *A&A*, 330, 1109
- Anders, E. & Grevesse, N. 1989, *Geochim. Cosmochim. Acta*, 53, 197
- Asplund, M. 2005, *ARA&A*, 43, 481
- Asplund, M., Grevesse, N., & Sauval, A. J. 2005, in *Astronomical Society of the Pacific Conference Series*, Vol. 336, *Cosmic Abundances as Records of Stellar Evolution and Nucleosynthesis*, ed. T. G. Barnes, III & F. N. Bash, 25
- Asplund, M., Grevesse, N., Sauval, A. J., & Scott, P. 2009, *ARA&A*, 47, 481
- Asplund, M., Nordlund, Å., Trampedach, R., & Stein, R. F. 1999, *A&A*, 346, L17
- Aurière, M. 2003, in *EAS Publications Series*, Vol. 9, *EAS Publications Series*, ed. J. Arnaud & N. Meunier, 105
- Bagnulo, S., Jehin, E., Ledoux, C., et al. 2003, *The Messenger*, 114, 10
- Ballester, P., Modigliani, A., Boitquin, O., et al. 2000, *The Messenger*, 101, 31
- Beers, T. C., Carollo, D., Ivezić, Z., et al. 2012, *ApJ*, 746, 34
- Belokurov, V., Zucker, D. B., Evans, N. W., et al. 2006, *ApJ*, 642, L137
- Bensby, T., Feltzing, S., & Lundström, I. 2004, *A&A*, 415, 155
- Benz, W. & Mayor, M. 1984, *A&A*, 138, 183
- Bergemann, M., Lind, K., Collet, R., Magic, Z., & Asplund, M. 2012, *MNRAS*, 427, 27
- Bruntt, H. 2009, *A&A*, 506, 235
- Bruntt, H., Basu, S., Smalley, B., et al. 2012, *MNRAS*, 423, 122
- Bruntt, H., Bedding, T. R., Quirion, P.-O., et al. 2010, *MNRAS*, 405, 1907
- Carollo, D., Beers, T. C., Lee, Y. S., et al. 2007, *Nature*, 450, 1020
- Chiappini, C., Matteucci, F., & Gratton, R. 1997, *ApJ*, 477, 765
- Chiavassa, A., Haubois, X., Young, J. S., et al. 2010, *A&A*, 515, A12
- Chiavassa, A., Plez, B., Josselin, E., & Freytag, B. 2009, *A&A*, 506, 1351
- Collet, R., Asplund, M., & Trampedach, R. 2007, *A&A*, 469, 687
- Creevey, O. L., Thévenin, F., Boyajian, T. S., et al. 2012, *A&A*, 545, A17
- de Laverny, P., Recio-Blanco, A., Worley, C. C., & Plez, B. 2012, *A&A*, 544, A126
- de Medeiros, J. R. & Mayor, M. 1999, *A&AS*, 139, 433
- de Medeiros, J. R., Silva, J. R. P., Do Nascimento, Jr., J. D., et al. 2006, *A&A*, 458, 895
- De Medeiros, J. R., Udry, S., Burki, G., & Mayor, M. 2002, *A&A*, 395, 97
- Dekker, H., D'Odorico, S., Kaufer, A., Delabre, B., & Kotzlowski, H. 2000, in *Society of Photo-Optical Instrumentation Engineers (SPIE) Conference Series*, Vol. 4008, *Society of Photo-Optical Instrumentation Engineers (SPIE) Conference Series*, ed. M. Iye & A. F. Moorwood, 534–545
- Diego, F., Charalambous, A., Fish, A. C., & Walker, D. D. 1990, in *Society of Photo-Optical Instrumentation Engineers (SPIE) Conference Series*, Vol. 1235, *Society of Photo-Optical Instrumentation Engineers (SPIE) Conference Series*, ed. D. L. Crawford, 562–576
- Donati, J., Semel, M., Carter, B. D., Rees, D. E., & Collier Cameron, A. 1997, *MNRAS*, 291, 658
- Edvardsson, B., Andersen, J., Gustafsson, B., et al. 1993, *A&A*, 275, 101
- Eggen, O. J., Lynden-Bell, D., & Sandage, A. R. 1962, *ApJ*, 136, 748
- Freeman, K. C. 2010, in *Galaxies and their Masks*, ed. D. L. Block, K. C. Freeman, & I. Puerari, 319
- Fuhrmann, K. 1998, *A&A*, 338, 161
- Gilmore, G., Randich, S., Asplund, M., et al. 2012, *The Messenger*, 147, 25
- Gilmore, G. & Reid, N. 1983, *MNRAS*, 202, 1025
- Gilmore, G., Wyse, R. F. G., & Kuijken, K. 1989, *ARA&A*, 27, 555
- Gray, D. F. 2005, *The Observation and Analysis of Stellar Photospheres*
- Gustafsson, B., Edvardsson, B., Eriksson, K., et al. 2008, *A&A*, 486, 951
- Heiter, U., Kupka, F., van't Veer-Menneret, C., et al. 2002, *A&A*, 392, 619
- Hekker, S. & Meléndez, J. 2007, *A&A*, 475, 1003
- Helmi, A. 2008, *A&A Rev.*, 15, 145
- Ivezić, Z., Beers, T. C., & Jurić, M. 2012, *ARA&A*, 50, 251
- Jofré, P., Panter, B., Hansen, C. J., & Weiss, A. 2010, *A&A*, 517, A57
- Jofré, P. & Weiss, A. 2011, *A&A*, 533, A59
- Kapteyn, J. C. & van Rhijn, P. J. 1920, *ApJ*, 52, 23
- Kaufer, A., Stahl, O., Tubbesing, S., et al. 2000, in *Society of Photo-Optical Instrumentation Engineers (SPIE) Conference Series*, Vol. 4008, *Society of Photo-Optical Instrumentation Engineers (SPIE) Conference Series*, ed. M. Iye & A. F. Moorwood, 459–466
- Kupka, F., Piskunov, N., Ryabchikova, T. A., Stempels, H. C., & Weiss, W. W. 1999, *A&AS*, 138, 119
- Kurucz, R. L. 1993, *VizieR Online Data Catalog*, 6039, 0
- Kurucz, R. L. 2005, *Memorie della Societa Astronomica Italiana Supplementi*, 8, 14
- Lebzelter, T., Heiter, U., Abia, C., et al. 2012, *A&A*, 547, A108
- Lee, Y. S., Beers, T. C., Sivarani, T., et al. 2008a, *AJ*, 136, 2022
- Lee, Y. S., Beers, T. C., Sivarani, T., et al. 2008b, *AJ*, 136, 2050
- Lind, K., Bergemann, M., & Asplund, M. 2012, *MNRAS*, 427, 50
- Luck, R. E. 1979, *ApJ*, 232, 797
- Luck, R. E. & Heiter, U. 2005, *AJ*, 129, 1063
- Luck, R. E. & Heiter, U. 2006a, *AJ*, 131, 3069
- Luck, R. E. & Heiter, U. 2006b, *AJ*, 131, 3069
- Magrini, L., Randich, S., Friel, E., et al. 2013, *ArXiv e-prints*
- Massarotti, A., Latham, D. W., Stefanik, R. P., & Fogel, J. 2008, *AJ*, 135, 209
- Masseron, T. 2006, PhD thesis, Observatoire de Paris, France
- Mayor, M., Pepe, F., Queloz, D., et al. 2003, *The Messenger*, 114, 20
- McWilliam, A. 1990, *ApJS*, 74, 1075
- Meléndez, J., Asplund, M., Alves-Brito, A., et al. 2008, *A&A*, 484, L21
- Mishenina, T. V. & Kovtyukh, V. V. 2001, *A&A*, 370, 951
- Molaro, P. & Monai, S. 2012, *A&A*, 544, A125
- Mucciarelli, A., Pancino, E., Lovisi, L., Ferraro, F. R., & Lapenna, E. 2013, *ArXiv e-prints*
- Nissen, P. E. 1981, *A&A*, 97, 145
- Pagel, B. E. J. & Tautvaisiene, G. 1998, *MNRAS*, 299, 535
- Pancino, E., Mucciarelli, A., Bonifacio, P., Monaco, L., & Sbordone, L. 2011, *A&A*, 534, A53
- Perryman, M. A. C., de Boer, K. S., Gilmore, G., et al. 2001, *A&A*, 369, 339
- Peterson, R. 1976, *ApJS*, 30, 61
- Plez, B. 2012, *Turbospectrum: Code for spectral synthesis*, astrophysics Source Code Library
- Ramírez, I. & Allende Prieto, C. 2011, *ApJ*, 743, 135
- Ramírez, I., Allende Prieto, C., & Lambert, D. L. 2007, *A&A*, 465, 271
- Recio-Blanco, A., Bijaoui, A., & de Laverny, P. 2006, *MNRAS*, 370, 141
- Reddy, B. E., Tomkin, J., Lambert, D. L., & Allende Prieto, C. 2003, *MNRAS*, 340, 304
- Reiners, A. & Schmitt, J. H. M. M. 2003, *A&A*, 412, 813
- Saar, S. H. & Osten, R. A. 1997, *MNRAS*, 284, 803
- Santos, N. C., Israelian, G., & Mayor, M. 2004, *A&A*, 415, 1153
- Sbordone, L., Bonifacio, P., Castelli, F., & Kurucz, R. L. 2004, *Memorie della Societa Astronomica Italiana Supplementi*, 5, 93
- Schönrich, R., Asplund, M., & Casagrande, L. 2011, *MNRAS*, 415, 3807
- Schröder, C., Reiners, A., & Schmitt, J. H. M. M. 2009, *A&A*, 493, 1099
- Schuler, S. C., King, J. R., Fischer, D. A., Soderblom, D. R., & Jones, B. F. 2003, *AJ*, 125, 2085
- Schuster, W. J., Moreno, E., Nissen, P. E., & Pichardo, B. 2012, *A&A*, 538, A21
- Siebert, A., Williams, M. E. K., Siviero, A., et al. 2011, *AJ*, 141, 187
- Smiljanic, R., Porto de Mello, G. F., & da Silva, L. 2007, *A&A*, 468, 679
- Snedden, C. A. 1973, PhD thesis, THE UNIVERSITY OF TEXAS AT AUSTIN.
- Soubiran, C. 1993, *A&A*, 274, 181
- Soubiran, C., Bienaymé, O., & Siebert, A. 2003, *A&A*, 398, 141
- Soubiran, C., Le Campion, J.-F., Cayrel de Strobel, G., & Caillo, A. 2010, *A&A*, 515, A111
- Sousa, S. G., Santos, N. C., Israelian, G., Mayor, M., & Monteiro, M. J. P. F. G. 2007, *A&A*, 469, 783
- Sousa, S. G., Santos, N. C., Mayor, M., et al. 2008, *A&A*, 487, 373
- Steinmetz, M., Zwitter, T., Siebert, A., et al. 2006, *AJ*, 132, 1645
- Stetson, P. B. & Pancino, E. 2008, *PASP*, 120, 1332
- Taberner, H. M., Montes, D., & González Hernández, J. I. 2012, *A&A*, 547, A13
- Thévenin, F. & Idiart, T. P. 1999, *ApJ*, 521, 753
- Tolstoy, E., Hill, V., & Tosi, M. 2009, *ARA&A*, 47, 371
- Torres, G., Fischer, D. A., Sozzetti, A., et al. 2012, *ApJ*, 757, 161
- Tull, R. G., MacQueen, P. J., Sneden, C., & Lambert, D. L. 1995, *PASP*, 107, 251
- Valenti, J. A. & Fischer, D. A. 2005, *ApJS*, 159, 141
- Valenti, J. A. & Piskunov, N. 1996, *A&AS*, 118, 595
- Villada, M. & Rossi, L. 1987, *Ap&SS*, 136, 351
- Vogt, S. S. 1987, *PASP*, 99, 1214
- Vogt, S. S., Allen, S. L., Bigelow, B. C., et al. 1994, in *Society of Photo-Optical Instrumentation Engineers (SPIE) Conference Series*, Vol. 2198, *Society of Photo-Optical Instrumentation Engineers (SPIE) Conference Series*, ed. D. L. Crawford & E. R. Craine, 362
- Wiese, W. L., Fuhr, J. R., & Deters, T. M. 1996, *Atomic transition probabilities of carbon, nitrogen, and oxygen : a critical data compilation*
- Worley, C. C., de Laverny, P., Recio-Blanco, A., et al. 2012, *A&A*, 542, A48
- Wu, Y., Singh, H. P., Prugniel, P., Gupta, R., & Koleva, M. 2011, *A&A*, 525, A71
- Zamanov, R. K., Bode, M. F., Melo, C. H. F., et al. 2008, *MNRAS*, 390, 377
- Zhao, G., Chen, Y.-Q., Shi, J.-R., et al. 2006, *Chinese J. Astron. Astrophys.*, 6, 265
- Zwitter, T., Siebert, A., Munari, U., et al. 2008, *AJ*, 136, 421

- 
- <sup>1</sup> LAB UMR 5804, Univ. Bordeaux – CNRS, 33270 Floirac, France
  - <sup>2</sup> Institute of Astronomy, University of Cambridge, Madingley Rd, Cambridge, CB3 0HA, U.K.
  - <sup>3</sup> Department of Physics and Astronomy, Uppsala University, Box 516, 75120 Uppsala, Sweden
  - <sup>4</sup> INAF-Osservatorio Astronomico di Bologna, Via Ranzani 1, 40127 Bologna, Italy
  - <sup>5</sup> ASI Science Data Center, I-00044 Frascati, Italy
  - <sup>6</sup> Max-Planck-Institut für Astrophysik, Karl-Schwarzschild-Str. 1, 85741 Garching, Germany
  - <sup>7</sup> INAF, Osservatorio Astronomico di Padova, Vicolo Osservatorio 5 Padova, 35122 Italy
  - <sup>8</sup> Dipartimento di Fisica e Astronomia, Università di Padova Padova, vicolo Osservatorio 3, 35122 Padova, Italy
  - <sup>9</sup> Instituto de Astrofísica de Canarias, 38200 La Laguna, Tenerife, Spain
  - <sup>10</sup> Laboratoire Lagrange (UMR7293), Univ. Nice Sophia Antipolis, CNRS, Observatoire de la Côte d’Azur, 06304 Nice, France
  - <sup>11</sup> INAF/Osservatorio Astrofisico di Arcetri, Largo Enrico Fermi 5 50125 Firenze, Italy
  - <sup>12</sup> Institut d’Astronomie et d’Astrophysique, U. Libre de Bruxelles, CP 226, Boulevard du Triomphe, 1050 Bruxelles, Belgium
  - <sup>13</sup> Dpto. Astrofísica, Facultad de CC. Físicas, Universidad Complutense de Madrid, E-28040 Madrid, Spain
  - <sup>14</sup> Dipartimento di Fisica & Astronomia, Università degli Studi di Bologna, Viale Berti Pichat 6/2, 40127 Bologna, Italy
  - <sup>15</sup> Department of Astronomy & Astrophysics, University of Chicago, Chicago, IL 60637, USA
  - <sup>16</sup> Centro de Astrofísica, Universidade do Porto, Rua das Estrelas, 4150-762 Porto, Portugal



**Table 4.** List of “golden” Fe I lines for various groups of stars (see text for definition of groups).

$\lambda$ [Å]	E [eV]	$\log gf$	Waals	Ref	MPD (2)	MPG (1)	FGDa (11)	FGDb (4)	FGKG (7)	MG (4)	$\psi$ Phe	KDa (2)	KDb (2)
4787.83	2.9980	-2.563	818.227	102					0.04/0.41 3/3			0.06/0.07 3/3	
4788.76	3.2370	-1.763	238.249	102			0.02/0.16 3/3	0.03/0.09 3/3	0.06/0.52 3/3			0.05/0.11 3/3	
4802.88	3.6420	-1.514	356.244	102								0.11/0.30 3/4	
4808.15	3.2510	-2.690	297.274	156			0.04/0.23 5/6	0.04/0.16 3/5	0.06/0.31 5/6	0.14/0.25 3/4		0.03/0.04 6/6	0.05/0.06 4/5
4869.46	3.5460	-2.420	246.248	156					0.06/0.65 3/3				
4875.88	3.3320	-1.920	848.231	156			0.07/0.39 4/4	0.08/0.21 3/4	0.04/0.51 4/4			0.13/0.15 3/4	0.08/0.21 3/3
4877.60	2.9980	-3.050	795.230	156					0.04/0.30 3/3			0.05/0.07 3/3	
4907.73	3.4300	-1.840	909.227	129			0.04/0.14 3/3		0.02/0.40 3/3			0.07/0.09 3/3	
4924.77	2.2790	-2.178	360.244	102		0.04 3		0.03/0.10 3/3					0.11/0.11 3/3
4946.39	3.3680	-1.170	848.232	187				0.04/0.13 3/3					
4950.11	3.4170	-1.670	880.228	129		0.02 4	0.07/0.22 3/5	0.03/0.14 4/5	0.06/0.16 3/4			0.14/0.16 4/4	0.05/0.16 3/5
4962.57	4.1780	-1.182	0.000	102			0.02/0.19 3/4	0.01/0.15 3/4				0.01/0.12 4/4	0.01/0.16 3/4
4969.92	4.2170	-0.710	962.279	129				0.01/0.16 3/3					0.03/0.10 3/3
4985.55	2.8650	-1.340	727.238	190		0.03 3							
4994.13	0.9150	-3.002	246.245	102	0.03/0.05 3/3	0.04 3		0.08/0.18 3/4					
5001.86	3.8810	-0.010	725.240	114		0.02 3							
5012.69	4.2830	-1.690	1020.279	156			0.05/0.20 3/4		0.07/0.30 3/4			0.06/0.11 4/4	
5044.21	2.8510	-2.038	713.238	102				0.04/0.11 3/3					
5049.82	2.2790	-1.349	353.239	102		0.01 3							
5058.50	3.6420	-2.830	353.313	167			0.09/0.20 3/5		0.09/0.22 4/5	0.15/0.40 3/4		0.12/0.28 4/4	
5060.08	0.0000	-5.431	0.000	102								0.17/0.29 3/3	0.08/0.08 3/3
5088.15	4.1540	-1.680	810.278	156					0.09/0.52 3/3				
5107.45	0.9900	-3.091	248.245	102		0.04 3							
5107.64	1.5570	-2.358	289.258	102		0.02 3							
5109.65	4.3010	-0.980	980.280	167								0.07/0.15 3/3	0.04/0.40 3/3
5127.36	0.9150	-3.278	243.246	102		0.03 3		0.05/0.16 3/3					
5131.47	2.2230	-2.515	356.274	102				0.03/0.17 3/3				0.11/0.34 3/3	0.09/0.09 3/3
5141.74	2.4240	-2.101	367.251	102		0.09 4	0.03/0.37 3/5	0.04/0.24 4/5				0.08/0.20 3/4	
5194.94	1.5570	-2.021	286.255	102		0.07 3							
5197.94	4.3010	-1.540	925.279	156			0.06/0.20 4/5	0.04/0.14 4/4	0.17/0.57 4/5			0.03/0.19 3/5	
5198.71	2.2230	-2.113	351.271	102		0.03 3		0.03/0.21 3/3					
5215.18	3.2660	-0.871	849.229	102		0.03 3							0.03/0.05 3/3
5217.39	3.2110	-1.116	815.232	102	0.03/0.07 3/3	0.05 4		0.07/0.18 3/4				0.09/0.23 3/4	
5223.18	3.6350	-1.783	390.253	102					0.05/0.34 3/3				
5225.53	0.1100	-4.755	207.253	102		0.04 4		0.04/0.27 3/4					0.11/0.21 4/4
5228.38	4.2200	-1.190	809.278	156								0.07/0.22 3/3	
5232.94	2.9400	-0.076	713.238	102	0.06/0.07 5/5	0.08 4							
5242.49	3.6340	-0.967	361.248	102		0.07 3		0.05/0.10 3/4				0.12/0.23 3/4	0.06/0.06 3/4
5243.78	4.2560	-1.050	842.278	156				0.00/0.25 4/4	0.13/0.46 3/4			0.07/0.09 4/4	0.04/0.05 3/4
5247.05	0.0870	-4.975	206.253	102		0.04 3						0.02/0.13 3/3	0.15/0.33 3/3
5250.21	0.1210	-4.918	207.253	102		0.03 3						0.13/0.20 3/3	0.10/0.10 3/3
5250.65	2.1980	-2.180	344.268	102	0.06/0.07 3/3	0.01 4		0.04/0.13 3/4	0.09/0.26 3/3			0.24/0.27 3/3	0.11/0.15 3/4
5253.02	2.2790	-3.840	368.253	156			0.03/0.13 4/5		0.06/0.26 4/5		0.51 3	0.06/0.09 5/5	
5253.46	3.2830	-1.573	849.229	102				0.04/0.20 3/3				0.17/0.19 3/3	
5285.13	4.4340	-1.540	1046.282	156					0.05/0.25 3/3			0.02/0.09 3/3	
5288.52	3.6940	-1.508	353.297	102								0.06/0.08 3/3	
5293.96	4.1430	-1.770	0.000	156			0.05/0.15 3/4	0.05/0.12 3/4	0.04/0.23 3/4			0.03/0.04 4/4	
5294.55	3.6400	-2.760	394.237	156			0.04/0.41 4/5		0.05/0.17 5/5			0.04/0.22 3/5	

Table 4. continued.

$\lambda$ [Å]	E [eV]	$\log gf$	Waals	Ref	MPD (2)	MPG (1)	FGDa (11)	FGDb (4)	FGKG (7)	MG (4)	$\psi$ Phe	KDa (2)	KDb (2)
5295.31	4.4150	-1.590	1014.281	156			0.03/0.19 3/5	0.02/0.11 4/5	0.04/0.21 5/5			0.05/0.09 5/5	0.06/0.18 3/3
5302.30	3.2830	-0.720	835.231	102		0.07 4							
5321.11	4.4340	-1.089	1024.281	102								0.03/0.10 3/3	
5322.04	2.2790	-2.802	341.236	102								0.07/0.10 3/3	0.02/0.04 3/3
5339.93	3.2660	-0.684	815.234	102		0.06 4							
5365.40	3.5730	-1.020	283.261	102		0.15 3		0.05/0.19 3/4			0.39 3	0.08/0.09 3/4	0.06/0.08 3/4
5367.47	4.4150	0.444	972.280	102		0.08 3							
5373.71	4.4730	-0.760	1044.282	156			0.03/0.12 3/4	0.00/0.08 3/4	0.06/0.27 3/4			0.09/0.18 4/4	
5379.57	3.6940	-1.514	363.249	102			0.01/0.13 3/4	0.02/0.25 3/4				0.06/0.08 4/4	0.01/0.11 3/4
5386.33	4.1540	-1.670	930.278	156			0.06/0.21 3/5	0.04/0.16 4/5	0.06/0.30 5/5		0.66 3	0.08/0.13 5/5	0.07/0.22 3/4
5389.48	4.4150	-0.410	959.280	187		0.06 3		0.02/0.07 3/4				0.08/0.09 3/4	0.02/0.04 3/4
5395.22	4.4450	-2.070	995.281	156					0.03/0.19 3/4		0.25 3	0.09/0.09 3/3	
5397.13	0.9150	-1.988	238.249	102	0.10/0.13 3/3								
5398.28	4.4450	-0.630	993.280	156			0.04/0.10 3/5	0.01/0.29 4/5	0.07/0.31 3/5		0.49 3	0.10/0.16 4/4	0.02/0.04 3/5
5412.78	4.4340	-1.716	971.280	102			0.01/0.12 3/4		0.03/0.18 4/4		0.17 3	0.03/0.05 3/4	
5415.20	4.3860	0.643	910.279	102		0.09 3							
5417.03	4.4150	-1.580	944.280	156			0.04/0.30 4/5	0.01/0.11 3/5	0.05/0.30 4/5			0.06/0.14 5/5	0.13/0.59 3/4
5424.07	4.3200	0.520	825.278	186	0.03/0.06 3/3	0.02 3							
5434.52	1.0110	-2.119	243.247	102	0.09/0.22 3/3								
5441.34	4.3120	-1.630	807.278	156			0.02/0.25 4/5		0.06/0.32 4/5	0.17/0.39 3/4		0.05/0.18 5/5	0.10/0.11 3/3
5445.04	4.3860	-0.020	895.279	186									0.03/0.04 3/3
5464.28	4.1430	-1.402	380.250	102					0.06/0.33 3/3			0.07/0.08 3/3	
5466.40	4.3710	-0.630	865.278	187				0.02/0.13 3/4	0.14/0.45 4/4			0.13/0.29 4/4	0.03/0.09 4/4
5470.09	4.4460	-1.710	953.280	156			0.05/0.13 3/4		0.05/0.25 3/4			0.07/0.09 3/4	0.08/0.12 3/3
5473.90	4.1540	-0.790	738.241	114								0.12/0.16 3/3	0.01/0.03 3/3
5483.10	4.1540	-1.406	737.241	102								0.06/0.08 3/3	
5487.15	4.4150	-1.430	908.279	156					0.13/0.37 3/3				
5494.46	4.0760	-1.990	0.000	156			0.01/0.24 3/4		0.08/0.33 4/4				
5522.45	4.2090	-1.450	744.215	156			0.02/0.09 3/4	0.02/0.09 3/4	0.06/0.31 4/4	0.06/0.23 3/4	0.27 3	0.05/0.05 4/4	0.01/0.13 3/4
5539.28	3.6420	-2.560	383.260	156			0.03/0.35 3/4		0.08/0.29 3/4			0.02/0.16 3/4	
5543.94	4.2170	-1.040	742.238	156			0.01/0.10 3/4	0.02/0.14 3/4	0.04/0.33 3/4		0.22 3	0.06/0.06 4/4	0.01/0.21 4/4
5546.51	4.3710	-1.210	825.278	156			0.05/0.10 3/4	0.04/0.17 3/4	0.06/0.33 3/4			0.05/0.06 4/4	
5560.21	4.4340	-1.090	895.278	156			0.03/0.10 3/4	0.03/0.20 3/4	0.06/0.28 3/4	0.02/0.20 3/4		0.05/0.07 4/4	0.01/0.01 3/3
5569.62	3.4170	-0.486	848.233	102	0.03/0.03 3/3	0.08 4							
5576.09	3.4300	-0.900	854.232	156	0.03/0.06 3/3	0.06 4		0.06/0.15 3/4					
5586.76	3.3680	-0.120	817.238	102		0.02 3							
5618.63	4.2090	-1.275	732.214	102			0.02/0.09 5/5	0.02/0.21 4/5	0.04/0.24 4/5			0.05/0.08 5/5	
5619.60	4.3860	-1.600	808.277	156			0.02/0.26 3/4	0.01/0.05 3/3	0.04/0.41 4/4			0.03/0.04 4/4	
5633.95	4.9910	-0.230	635.270	156			0.02/0.18 3/4	0.01/0.18 3/4	0.08/0.42 3/4			0.04/0.07 4/4	0.03/0.13 3/4
5636.70	3.6400	-2.510	368.310	156			0.02/0.33 3/4		0.02/0.27 4/4			0.03/0.04 4/4	
5638.26	4.2200	-0.770	730.235	156			0.03/0.17 4/5	0.03/0.17 4/5	0.09/0.41 4/5			0.05/0.09 4/5	0.02/0.13 5/5
5641.43	4.2560	-1.080	739.234	156			0.01/0.28 3/3					0.03/0.05 3/3	
5649.99	5.0990	-0.820	719.265	156					0.04/0.24 3/3			0.02/0.04 3/3	
5651.47	4.4730	-1.900	898.278	156			0.04/0.17 5/6		0.04/0.18 6/6	0.12/0.20 3/4		0.04/0.05 5/6	
5652.32	4.2600	-1.850	754.210	156			0.05/0.22 4/5		0.02/0.27 4/5			0.04/0.04 5/5	0.10/0.28 3/3
5653.87	4.3860	-1.540	792.277	156			0.01/0.13 3/3		0.01/0.14 3/3			0.02/0.10 3/3	0.04/0.04 3/3
5655.18	5.0640	-0.600	0.000	156								0.08/0.27 3/3	
5661.35	4.2840	-1.756	765.209	102			0.03/0.10 3/4		0.02/0.20 3/4			0.04/0.08 4/4	
5662.52	4.1780	-0.573	724.235	102		0.06 4	0.04/0.22 3/5	0.04/0.24 4/5	0.10/0.25 3/4			0.14/0.28 4/4	0.06/0.14 3/5

Table 4. continued.

$\lambda$ [Å]	E [eV]	$\log gf$	Waals	Ref	MPD (2)	MPG (1)	FGDa (11)	FGDb (4)	FGKG (7)	MG (4)	$\psi$ Phe	KDa (2)	KDb (2)
5679.02	4.6520	-0.820	1106.291	156			0.04/0.12 5/5	0.03/0.30 4/5	0.08/0.26 5/5			0.05/0.07 5/5	0.04/0.11 4/4
5691.50	4.3010	-1.420	746.231	156								0.02/0.04 3/3	
5696.09	4.5480	-1.720	965.279	102					0.01/0.28 3/4			0.03/0.07 3/3	
5698.02	3.6400	-2.580	385.252	156					0.01/0.22 3/3				
5701.54	2.5590	-2.160	361.237	102		0.06 4	0.05/0.28 4/5		0.10/0.28 3/3			0.09/0.11 4/4	0.06/0.16 4/5
5705.46	4.3010	-1.355	744.231	102			0.04/0.11 4/5		0.03/0.23 5/5	0.12/0.49 3/4	0.48 3	0.04/0.06 5/5	0.03/0.16 4/5
5731.76	4.2560	-1.200	727.232	156			0.02/0.15 5/5	0.02/0.15 4/5	0.09/0.38 4/5		0.58 3	0.03/0.06 5/5	0.03/0.07 4/5
5732.30	4.9910	-1.460	613.275	156					0.02/0.11 4/5	0.11/0.18 3/4		0.04/0.10 4/4	
5741.85	4.2560	-1.672	725.232	102			0.03/0.17 5/6		0.05/0.25 6/6	0.07/0.23 3/4	0.62 3	0.03/0.06 6/6	0.05/0.17 4/5
5760.34	3.6420	-2.390	386.250	156								0.03/0.07 3/3	
5775.08	4.2200	-1.297	720.231	102					0.07/0.34 5/6	0.04/0.39 3/5			0.05/0.07 5/5
5778.45	2.5880	-3.430	361.237	102					0.06/0.27 4/6	0.03/0.44 3/4			0.04/0.10 4/4
5784.66	3.3960	-2.532	796.244	102					0.05/0.42 3/3				
5849.68	3.6940	-2.890	379.305	156					0.02/0.10 3/4	0.09/0.13 3/4		0.02/0.02 3/3	
5853.15	1.4850	-5.180	0.000	156					0.02/0.16 3/4			0.03/0.05 3/3	
5855.08	4.6080	-1.478	962.279	102			0.03/0.17 5/6		0.04/0.33 5/6	0.14/0.49 3/5		0.04/0.11 5/6	
5858.78	4.2200	-2.160	786.278	156					0.01/0.09 3/4	0.02/0.18 3/3		0.02/0.08 3/3	
5883.82	3.9600	-1.260	998.250	156			0.01/0.15 3/4	0.01/0.12 3/3				0.06/0.07 3/4	0.03/0.08 3/3
5902.47	4.5930	-1.710	227.252	156					0.06/0.19 3/4			0.11/0.26 3/3	
5905.67	4.6520	-0.690	994.282	156			0.01/0.16 4/5	0.02/0.15 4/5				0.06/0.21 4/4	0.03/0.16 3/3
5927.79	4.6520	-0.990	984.281	156			0.02/0.09 3/4		0.05/0.16 3/4	0.14/0.46 3/4	0.39 3	0.04/0.05 3/4	0.01/0.08 3/3
5929.68	4.5480	-1.310	864.275	156			0.02/0.14 3/4		0.03/0.76 3/4			0.03/0.05 3/4	0.03/0.04 3/3
5930.18	4.6520	-0.230	983.281	187		0.07 3	0.04/0.19 3/5	0.01/0.13 3/5	0.06/0.17 3/5			0.14/0.19 3/4	0.02/0.05 4/4
5934.65	3.9280	-1.070	959.247	156			0.02/0.18 3/4	0.01/0.20 3/4	0.03/0.30 3/4			0.11/0.15 4/4	0.03/0.07 3/3
5956.69	0.8590	-4.553	227.252	102		0.04 4						0.03/0.10 4/5	0.03/0.16 4/4
6003.01	3.8810	-1.120	898.241	187				0.03/0.20 3/4				0.16/0.31 3/3	0.06/0.10 3/3
6012.21	2.2230	-4.038	309.270	102								0.03/0.05 3/4	0.04/0.12 3/4
6027.05	4.0760	-1.089	380.250	102			0.04/0.10 4/5	0.03/0.11 3/5	0.06/0.14 3/5			0.06/0.27 5/5	0.02/0.16 4/4
6065.48	2.6080	-1.470	354.234	102	0.03/0.05 4/4	0.05 4		0.04/0.29 3/5					0.09/0.34 3/4
6079.01	4.6520	-1.020	920.276	156			0.01/0.18 3/4	0.02/0.19 3/4	0.05/0.11 3/4			0.02/0.03 3/4	0.02/0.08 3/3
6093.64	4.6070	-1.400	866.274	156			0.01/0.06 3/4		0.02/0.07 3/4	0.05/0.20 3/3		0.03/0.04 3/4	
6094.37	4.6520	-1.840	914.276	156					0.03/0.32 3/4			0.03/0.13 3/3	
6096.66	3.9840	-1.830	963.250	156			0.03/0.23 4/5	0.02/0.08 4/4	0.04/0.18 4/5			0.04/0.14 5/5	0.03/0.08 3/4
6127.91	4.1430	-1.399	0.000	102								0.10/0.27 3/3	
6136.99	2.1980	-2.941	280.265	102		0.02 3	0.05/0.37 3/4					0.05/0.12 3/4	0.02/0.07 3/3
6151.62	2.1760	-3.312	277.263	102			0.03/0.10 5/5	0.01/0.15 4/4	0.01/0.83 3/5	0.13/0.78 3/4	0.65 4	0.06/0.07 4/5	0.03/0.14 4/5
6165.36	4.1430	-1.473	380.250	102			0.02/0.18 4/5	0.01/0.07 3/5	0.05/0.64 4/5	0.15/0.32 3/4		0.04/0.06 5/5	0.04/0.16 4/5
6173.33	2.2230	-2.880	281.266	102		0.05 4	0.03/0.12 4/5	0.02/0.13 4/5	0.06/0.21 3/4	0.19/0.78 3/4		0.08/0.20 4/5	0.06/0.12 3/4
6187.99	3.9430	-1.620	903.244	156			0.03/0.22 5/6	0.02/0.20 5/6	0.05/0.65 5/6			0.04/0.21 6/6	0.03/0.08 4/5
6200.31	2.6080	-2.405	350.235	102		0.07 3	0.01/0.13 3/4	0.02/0.09 3/4	0.02/0.20 3/4			0.08/0.10 3/4	0.07/0.29 3/3
6219.28	2.1980	-2.434	278.264	102		0.02 4	0.02/0.40 3/5	0.04/0.26 3/5	0.02/0.28 3/3		0.10 3	0.09/0.17 3/4	0.05/0.07 4/4
6226.73	3.8830	-2.120	845.244	156			0.01/0.25 4/5		0.03/0.62 4/5			0.03/0.05 3/5	
6240.65	2.2230	-3.203	301.272	102								0.09/0.38 3/3	
6246.32	3.6020	-0.805	820.246	102	0.01/0.05 3/4	0.06 5		0.06/0.18 4/6	0.04/0.21 4/4		0.22 3	0.23/0.34 3/4	0.06/0.31 5/5
6252.56	2.4040	-1.727	326.245	102	0.02/0.05 5/5	0.04 5	0.07/0.26 4/6	0.07/0.14 3/6	0.09/0.26 3/4		0.37 3	0.17/0.19 3/4	0.11/0.35 3/5
6265.13	2.1760	-2.545	274.261	102		0.03 4	0.03/0.34 4/5	0.03/0.29 4/5	0.02/0.25 3/4			0.12/0.17 4/5	0.09/0.65 4/5
6270.22	2.8580	-2.536	350.249	102			0.03/0.29 4/5	0.03/0.17 3/5	0.06/0.76 4/5			0.04/0.05 4/5	0.02/0.27 4/5
6271.28	3.3320	-2.703	720.247	102			0.04/0.28 3/4		0.04/0.20 3/4			0.03/0.07 3/4	
6297.79	2.2230	-2.702	278.264	102		0.04 3		0.04/0.15 3/4				0.15/0.18 4/4	0.08/0.19 3/4

**Table 4.** continued.

$\lambda$ [Å]	E [eV]	$\log gf$	Waals	Ref	MPD (2)	MPG (1)	FGDa (11)	FGDb (4)	FGKG (7)	MG (4)	$\psi$ Phe	KDa (2)	KDb (2)
6301.50	3.6540	-0.718	0.000	102		0.09 3							
6315.81	4.0760	-1.610	410.250	156			0.02/0.35 3/4	0.04/0.21 3/3	0.05/0.18 3/4			0.05/0.10 4/4	0.02/0.53 3/4
6322.69	2.5880	-2.448	345.238	102			0.02/0.32 4/5	0.02/0.24 4/5	0.08/0.24 3/4		0.31 3	0.08/0.20 4/4	0.02/0.18 4/5
6335.33	2.1980	-2.177	275.261	102	0.03/0.09 3/3	0.05 4	0.03/0.14 3/5	0.05/0.15 3/5	0.08/0.28 3/3	0.23/0.27 3/3		0.18/0.22 3/3	0.12/0.28 4/4
6336.82	3.6860	-0.856	845.240	102		0.06 5	0.06/0.28 3/6	0.05/0.26 5/6	0.11/0.18 4/5	0.24/0.65 3/4	0.13 3		0.05/0.26 4/5
6393.60	2.4330	-1.504	326.246	102	0.04/0.07 5/5	0.06 5	0.05/0.23 3/5	0.07/0.45 4/5	0.12/0.24 3/4		0.51 3		0.14/0.18 3/4
6411.65	3.6540	-0.656	820.247	102	0.03/0.06 4/5	0.05 5		0.06/0.12 4/6	0.04/0.26 3/4		0.51 3		0.11/0.42 4/5
6430.85	2.1760	-1.976	271.257	102	0.02/0.05 5/5	0.05 5	0.03/0.45 3/6	0.05/0.13 3/6	0.10/0.25 3/4		0.51 3	0.18/0.29 3/4	
6481.87	2.2790	-2.985	308.243	102		0.03 4	0.02/0.42 4/5	0.02/0.41 3/5	0.07/0.28 3/4			0.04/0.10 3/5	0.00/0.07 3/4
6494.98	2.4040	-1.256	321.247	102	0.03/0.08 3/3	0.04 3							
6496.47	4.7950	-0.530	925.279	156					0.07/0.37 3/4			0.03/0.08 3/4	0.01/0.02 3/3
6498.94	0.9580	-4.688	226.253	102		0.06 4						0.11/0.11 4/5	0.04/0.23 3/4
6533.93	4.5580	-1.360	908.277	156					0.01/0.07 3/4			0.02/0.03 3/4	
6574.23	0.9900	-5.013	0.000	102								0.08/0.13 3/4	0.04/0.16 3/4
6593.87	2.4330	-2.394	321.247	102		0.03 3	0.01/0.15 3/4	0.03/0.09 3/4	0.03/0.26 3/3			0.08/0.11 4/4	0.09/0.23 3/3
6597.56	4.7950	-0.970	893.276	156			0.01/0.18 3/4	0.02/0.14 3/4				0.02/0.19 3/4	0.04/0.05 3/3
6609.11	2.5590	-2.676	335.245	102		0.04 3	0.02/0.42 3/4	0.04/0.17 3/4	0.09/0.28 3/3			0.05/0.06 3/3	0.02/0.38 3/4
6627.54	4.5480	-1.580	754.209	156								0.02/0.13 3/3	
6648.08	1.0110	-5.918	229.254	102							0.50 3	0.02/0.04 3/3	
6699.14	4.5930	-2.101	297.273	102					0.05/0.14 4/5			0.04/0.07 3/4	
6703.57	2.7580	-3.060	320.264	156			0.04/0.11 3/4					0.02/0.03 3/3	
6713.74	4.7950	-1.500	857.272	156					0.01/0.44 3/4			0.04/0.05 3/3	
6739.52	1.5570	-4.794	256.244	102					0.01/0.67 3/4			0.01/0.03 3/3	
6750.15	2.4240	-2.604	335.241	102		0.03 3	0.03/0.14 3/4				1.09 3	0.07/0.07 3/4	0.03/0.05 3/3
6810.26	4.6070	-0.986	873.275	102					0.05/0.43 3/4				0.02/0.12 3/3

Column descriptions:  $\lambda$ : wavelength.  $E_{\text{low}}$ : lower level energy. “Waals”: parameters used to calculate line broadening due to collisions with neutral hydrogen; integer part: broadening cross-section at a velocity of  $10^4$  m s $^{-1}$  in atomic units, fractional part: velocity parameter (see ?); if zero, the Unsöld approximation was used. “Ref”: reference code for the  $gf$ -values (see below). The remaining columns are headed by a label for each group defined in the text, and the number of stars in parantheses. The columns give, for each group, the minimum and maximum standard deviations of the average line abundances, and the minimum and maximum number of abundances averaged for each line.

References: 102: ????????. 114: ???. 129: ???. 156: ?. 167: ???. 186: ???. 187: ???.

**Table 5.** List of “golden” Fe II lines for various groups of stars (see text for definition of groups).

$\lambda$ [Å]	E [eV]	$\log gf$	Waals	Ref	MPD (2)	MPG (1)	FGD <sup>†</sup> (15)	FGKG (7)	MG (4)	KD <sup>‡</sup> (1)
4923.93	2.8910	-1.260	175.202	158	0.16/0.25 4/4					
4993.36	2.8070	-3.684	172.220	166		0.04 3	0.00/0.21 3/4	0.13/0.64 3/4		0.29 4
5264.81	3.2300	-3.130	186.300	158						0.09 3
5325.55	3.2210	-3.160	179.252	158						0.08 3
5414.07	3.2210	-3.580	185.303	158			0.01/0.07 3/4	0.07/0.24 3/4		0.08 3
5425.26	3.1990	-3.220	178.255	158		0.14 3	0.01/0.14 4/5	0.09/0.35 4/5	0.17/0.50 3/5	0.11 5
5534.85	3.2450	-2.865	178.239	166						0.06 3
5991.38	3.1530	-3.647	172.221	166			0.01/0.12 3/4			0.04 3
6084.11	3.1990	-3.881	173.223	166				0.08/0.20 3/4		0.03 3
6247.56	3.8920	-2.435	186.272	166						0.04 3
6432.68	2.8910	-3.570	169.204	158		0.07 3	0.01/0.32 3/4	0.02/0.07 3/4	0.10/0.19 3/4	0.05 3
6456.38	3.9030	-2.185	185.276	166		0.14 4	0.03/0.19 4/5	0.04/0.38 4/5	0.14/0.24 4/4	0.03 5

Column descriptions:  $\lambda$ : wavelength.  $E_{\text{low}}$ : lower level energy. “Waals”: parameters used to calculate line broadening due to collisions with neutral hydrogen; integer part: broadening cross-section at a velocity of  $10^4$  m s<sup>-1</sup> in atomic units, fractional part: velocity parameter (see ?); if zero, the Unsöld approximation was used. “Ref”: reference code for the  $gf$ -values (see below). The remaining columns are headed by a label for each group defined in the text, and the number of stars in parantheses. The columns give, for each group, the minimum and maximum standard deviations of the average line abundances, and the minimum and maximum number of abundances averaged for each line.

Notes: <sup>†</sup> 5414.07Å was not used in  $\mu$  Cas, and 5991.38Å not in HD 49933. <sup>‡</sup> The column marks the lines used for  $\epsilon$  Eri; of these, only 4993.36Å and 6456.38Å were used in 61 Cyg A and Gmb 1830; only 4993.36Å and 5425.26Å in 61 Cyg B.

References: 158: ?. 166: ?.